



OPEN ACCESS

EDITED BY

Huade Guan,
Flinders University, Australia

REVIEWED BY

Eduardo Landulfo,
Instituto de Pesquisas Energéticas e Nucleares
(IPEN), Brazil
Jianhui Bai,
Chinese Academy of Sciences (CAS), China

*CORRESPONDENCE

José Luis Flores-Rojas,
✉ jlflores@igp.gob.pe

RECEIVED 12 March 2024

ACCEPTED 19 July 2024

PUBLISHED 13 August 2024

CITATION

Fashé-Raymundo O, Flores-Rojas JL,
Estevan-Arredondo R, Giráldez-Solano L,
Suárez-Salas L, Sanabria-Pérez E, Karam HA
and Silva Y (2024) Observational
characterization and empirical modeling of
global, direct and diffuse solar irradiances at
the Peruvian central Andes.
Front. Earth Sci. 12:1399971.
doi: 10.3389/feart.2024.1399971

COPYRIGHT

© 2024 Fashé-Raymundo, Flores-Rojas,
Estevan-Arredondo, Giráldez-Solano,
Suárez-Salas, Sanabria-Pérez, Karam and
Silva. This is an open-access article distributed
under the terms of the [Creative Commons
Attribution License \(CC BY\)](https://creativecommons.org/licenses/by/4.0/). The use,
distribution or reproduction in other forums is
permitted, provided the original author(s) and
the copyright owner(s) are credited and that
the original publication in this journal is cited,
in accordance with accepted academic
practice. No use, distribution or reproduction
is permitted which does not comply with
these terms.

Observational characterization and empirical modeling of global, direct and diffuse solar irradiances at the Peruvian central Andes

Octavio Fashé-Raymundo¹, José Luis Flores-Rojas^{2*},
René Estevan-Arredondo², Lucy Giráldez-Solano²,
Luis Suárez-Salas², Elias Sanabria-Pérez³, Hugo Abi Karam⁴ and
Yamina Silva²

¹Universidad Nacional Mayor de San Marcos, Lima, Peru, ²Instituto Geofísico del Perú, Lima, Peru,

³Universidad Nacional del Centro del Perú, Facultad de Ingeniería Química, Huancayo, Peru,

⁴Universidade Federal de Rio de Janeiro, Rio de Janeiro - Universidade Federal de Rio de Janeiro/Instituto de Geociências/Centro de Ciências Matemáticas e da Natureza, Rio de Janeiro, Brazil

The present study aims to comprehensively assess the solar irradiance patterns in the western zone of the Mantaro Valley, a region of ecological and agricultural significance in the central Peruvian Andes. Leveraging radiation data from the Baseline surface Radiation Network (*BSRN*) sensors located in the Huancayo Geophysical Observatory (*HYGO*-12.04°S,75.32°W, 3350 masl) spanning from 2017 to 2022, the research delves into the seasonal variations and trends in surface solar irradiance components. Actually, the study investigates the diurnal and seasonal variations of solar irradiance components, namely diffuse (E_{DF}), direct (E_{DR}), and global (E_G) irradiance. Results demonstrate distinct peaks and declines across seasons, with E_{DR} and E_{DF} exhibiting opposing seasonal trends, influencing the overall variability in E_G . Peaks of E_G occurred in spring (3.32 MJ m⁻² h⁻¹ at noon), particularly during October (24.14 MJ m⁻² day⁻¹), probably associated with biomass-burning periods and heightened aerosol optical depth (*AOD*). These findings highlight the impact of biomass-burning aerosols on solar radiation dynamics in the region. In general, the seasonal variability of E_G on the *HYGO* is lower than that observed in other regions of South America at higher latitudes and reach its maximums during spring months. Moreover, the research evaluates various irradiance models to establish correlations between sunshine hours, measured with a solid glass sphere heliograph, and E_G and E_{DF} at different time scales, showing acceptable accuracy to predict. In addition, the sigmoid logistic function emerges as the most effective in correlating the hourly diffuse fraction (K_D^h) and the hourly clearness index (K_T^h), showcasing superior performance compared to alternative functions and exhibiting strong statistical significance and providing valuable insights for future solar radiation forecasting and modeling efforts. This study offers valuable insights for solar radiation forecasting and modeling

efforts, emphasizing the importance of interdisciplinary research for solar power generation, sustainable development and climate resilience in mountainous regions like the Peruvian Andes.

KEYWORDS

solar irradiance models, global irradiance, diffuse irradiance, direct irradiance, peruvian central Andes

1 Introduction

Solar radiation serves as the primary energy source driving surface-atmosphere interactions, influencing a wide array of physical, chemical, and biological processes within Earth's atmospheric and oceanic systems (Munner, 2004a; Arya, 2005). Understanding the components of solar radiation, namely global (E_G), diffuse (E_{DF}), and direct (E_{DR}) radiation at the surface, is indispensable for various applications. These include identifying regions suitable for solar power generation (Janjai et al., 2009; Della-Ceca et al., 2019; Barragán-Escandón et al., 2022), assessing energy consumption in buildings (Rodríguez-Hidalgo et al., 2012; Albarracín, 2017), supporting ecophysiological studies (Woodward and Sheeh, 1983; Monteith and Unsworth, 1990) estimating crop evapotranspiration (Supit and Van Kappel, 1998), and facilitating urban planning (Redweik et al., 2013).

Since 1990, global organizations have emphasized the environmental risks posed by fossil fuels, promoting renewable energy. However, global energy demand is projected to rise by over 50% by 2030 (Sayigh, 2020). In recent decades, there has been a notable surge in investment and development of alternative technologies aimed at producing clean energy from renewable sources. These technologies offer lower environmental impacts compared to traditional ones, garnering significant attention worldwide (Ellabban et al., 2014). The “Renewable Energy Policy Network for the 21st Century Report” highlights a growing interest in renewable energies, with a global push towards achieving net-zero emissions by 2050 (REN21, 2023). Currently, solar and wind power are among the most promising and feasible renewable resources. The implementation of photovoltaic systems (PV) has particularly seen a rapid expansion, with growth rates reaching 40% in recent years (Jager Waldau, 2019).

In this context, observations of solar radiation are commonly focused on global radiation. However, many applications require data on irradiation on sloping surfaces. Therefore, it is often necessary to divide global radiation into its beam and diffuse components to derive the specific data needed from the available global radiation measurements. A number of diffuse fraction models are available for averaging times ranging from 1 month to 1 hour or even less. Different diffuse fraction models generally require varying input data. The model proposed by Erbs et al. (1982) only needs the hourly clearness index. The models of Maxwell (1987) and Skartveit and Olseth (1987) require both the hourly clearness index and solar elevation and the model of Skartveit et al. (1998) which added hour-to-hour variability index and regional surface albedo.

Furthermore, the model by Perez et al. (1992) further includes ambient dew-point temperature and an hour-to-hour variability index. From a large multiclimate database, they derived a computationally efficient model using a four-dimensional look-up

table consisting of a $6 \times 6 \times 5 \times 7$ matrix of numerical constants. Moreover, Ridley et al. (2010) developed a multiple predictor model that uses hourly clearness index, daily clearness index, solar altitude, apparent solar time and a measure of persistence of global radiation level as predictors. This model performs marginally better than currently used models for locations in the Northern Hemisphere and substantially better for Southern Hemisphere locations.

In general, South America lacks sufficient radiometric stations equipped to measure various components of solar radiation, typically only measuring global radiation (E_G) and sunshine hours (S). However, comprehensive data on diffuse radiation (E_{DF}) incident on tilted surfaces is essential for various applications, including hydrological, architectural (thermal comfort), urban planning, and micro-meteorological studies. Moreover, such data supports the design of solar energy systems, aiding in the optimization of solar collector configurations and the determination of optimal tilt angles and panel orientations to maximize energy conversion efficiency. This problem is particularly serious in Andean regions, due to the lack of high quality radiometric sensors like BSRN stations Driemel et al. (2018). Actually, there are studies which compare global irradiance data with numerical irradiance models for the south-central region of Chile (Álvarez et al., 2011), Argentina (Podestá et al., 2004; Ceballos et al., 2022) and spectral irradiance measurements in the high Andes of Peru (Hastenrath, 1997).

Moreover, compared to 1980, projections indicate a decrease in ultraviolet UV-B irradiance by 5%–20% at mid to high latitudes by the end of the 21st century, while a slight increase of 2%–3% is expected in low latitudes. The tropics (25°N–25°S) exhibit low seasonal variability, with naturally low ozone levels around 250 Dobson Units contributing to high UV radiation. Notably, there have been no significant changes in total ozone column over this period in this region (McKenzie et al., 2011). Additionally, factors contributing to heightened UV radiation levels include the altitude of mountainous regions, clear skies, and low aerosol concentrations, notably observed in the Andean mountains between 12°S and 23°S, which boast over 100 peaks exceeding 6000 m above sea level (Blumthaler et al., 1997; Cordero et al., 2014). This phenomenon has been investigated in various locations, including the Chilean Andes (Piazana, 1996), Bolivian Andes (Zaratti et al., 2003), and Argentinian Andes (Cede et al., 2002; Luccini et al., 2006).

Particularly, UV solar irradiance measurements were conducted by Suárez Salas et al. (2017) in the Peruvian central Andes, at the HYGO, between January 2003 and December 2006, using a GUV-511 multi-channel filter radiometer. Data analysis revealed daily, monthly, and annual cycles of UV solar irradiance at four wavelengths (305, 320, 340, and 380 nm). Clear sky and all sky conditions were distinguished, with February showing peak values. The highest hourly mean UV Index at noon reached 18.8 under clear

sky conditions and 15.5 under all sky conditions, with outlier peaks close to 28. Cloud cover increased spectral irradiance at 340 nm by up to 20%, indicating exceptionally high levels of UV radiation in the tropical central Andes. However, to date, there are no studies aimed at studying solar radiation in the central Peruvian Andes with high quality data.

On the other hand, in Brazil, several studies have investigated solar radiation patterns for different sites using high quality radiometric sensors like BSRN stations (Driemel et al., 2018). For instance, Oliveira et al. (2002b) examines seasonal variations in E_G and E_{DR} diurnal patterns using surface data from São Paulo. Codato et al. (2008) conducted a comparative analysis of solar radiation fields between São Paulo and Botucatu. Ferreira et al. (2012) focused on São Paulo's radiation balance, highlighting atmospheric factors' role in E_G seasonal variability. Furthermore, Pereira et al. (2006) and Martins et al. (2007) utilized SOLAS network data to validate a satellite-derived model, shedding light on Brazil's solar energy potential. In a related study in Rio de Janeiro City, Marques Filho et al. (2016) obtained daily maximum values of E_G during summer and minimums in winter, showing higher values compared to a similar analysis in São Paulo City. This difference, despite both cities being within the same latitude range, can be attributed to the influence of cloudiness and marine aerosols in Rio de Janeiro City, which affect the components and balance of solar radiation at the surface. Additionally, De Souza et al. (2016) presented the seasonal variation of E_G in Alagoas city, while Gomes et al. (2022) analyzed the seasonal variation of both E_G and E_{DF} in San Salvador city.

The present study aims to comprehensively analyze solar irradiance patterns in the western Mantaro Valley, utilizing data from BSRN sensors at the Huancayo Geophysical Observatory (HYGO), spanning 2017 to 2022, the research investigates seasonal variations and trends in surface solar irradiance components. Specifically, the study explores diurnal and seasonal fluctuations of diffuse (E_{DF}), direct (E_{DR}), and global (E_G) irradiance. In addition, the research evaluates various irradiation models to establish correlations between solar irradiance parameters, aiming to predict E_G and E_{DF} accurately across different time scales. The description of the site is shown in Section 2, sensors and instrumentation are described in Section 3, database and methodologies used in the study are presented in Section 4. Section 5 summarized the results of the research, including observational characterization and empirical models of global, direct and diffuse solar irradiances, Section 6 discuss the main contributions of the research and finally, Section 7 concludes the paper.

2 Site and location

The measurements in this study were conducted at the Huancayo Geophysical Observatory (HYGO), situated at coordinates 12.04°S latitude and 75.32°W longitude, with an elevation of 3350 m above sea level (m.a.s.l.). HYGO is operated by the Geophysical Institute of Peru (IGP). It is located within the Mantaro River Basin (MRB) within the central Peruvian Andes, covering a vast drainage area spanning 34,550 square kilometers (Figure 1A). The MRB encompasses various regions of the central Andes, including Junin, Ayacucho, Huancavelica, and Pasco, with elevations ranging

from 500 to 5,300 m.a.s.l. and a mean altitude of approximately 3870 m.a.s.l. (Figure 1B). Furthermore, HYGO is situated within the non-irrigated agricultural expanse of the Mantaro Valley (MV), positioned at a distance of 7 km from the Mantaro River and 12 km from the city of Huancayo. The observatory is nestled between the Western Andes and the Huaytapallana cordillera to the east, (Figure 1A).

The climatological data spanning 48 years (1965–2013) from HYGO reveals a predominant unimodal seasonal pattern in precipitation. This pattern distinctly delineates a dry season extending from April to August, followed by a rainy season spanning from September to March. Notably, the latter part of August may witness intense rainfall events, with precipitation steadily increasing until it reaches its zenith during the austral summer, specifically in January through March, as substantiated by prior studies (Silva et al., 2008; Espinoza-Villar et al., 2009). Following this period, a noteworthy decline in precipitation is observed in April. Consequently, approximately 83% of the annual accumulated rainfall occurs during the rainy season, as documented in earlier research (Silva et al., 2010).

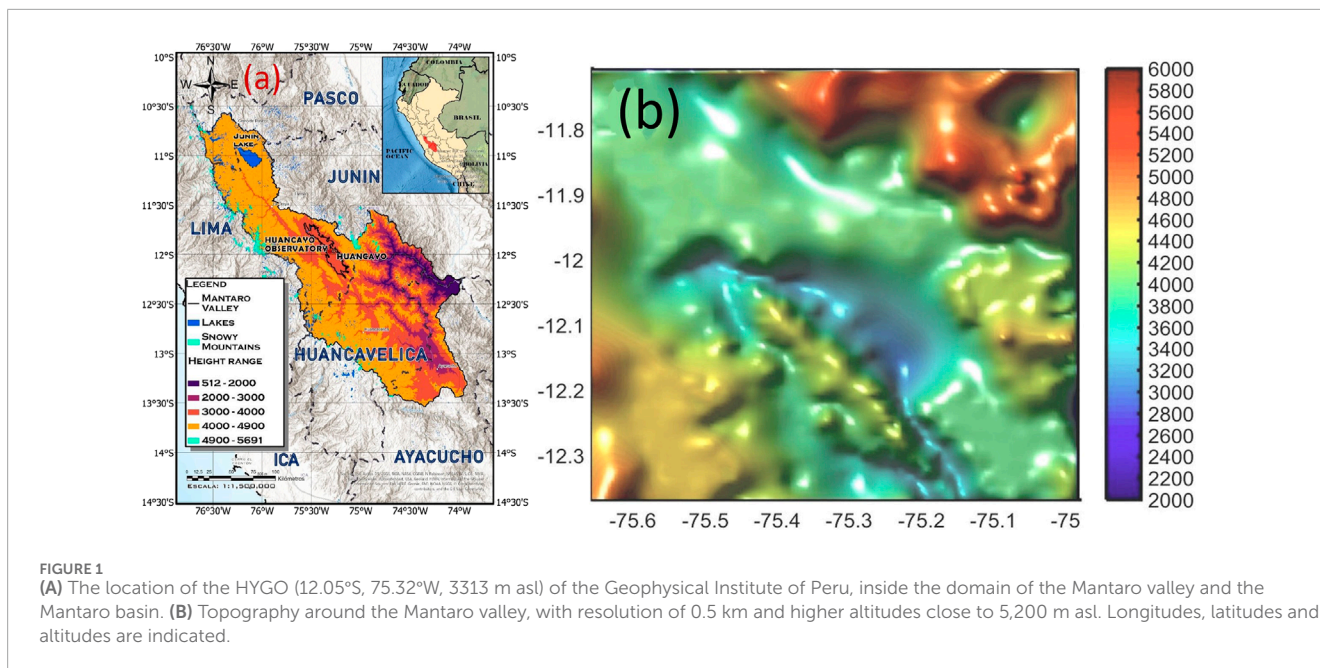
Moreover, Flores-Rojas et al. (2019a) shows that the components of the energy budget exhibit both seasonal and daily variations, with the partitioning of net irradiance (Q^N) into turbulent sensible (Q_H), turbulent latent (Q_E) heat fluxes, and soil heat flux (Q_G) being influenced by the dynamic interplay between the soil and the atmosphere's heat transport capabilities, as well as the physical attributes of the surface. At solar noon, the mean monthly Q^N attains its peak in November, registering at 660 W m^{-2} , while reaching its nadir in July at 450 W m^{-2} .

During the fall and winter months, the mean monthly Q_H , peaking around 300 W m^{-2} at noon, surpasses the mean monthly Q_E , which reaches its maximum of approximately 100 W m^{-2} at the same time. This discrepancy can be attributed to the limited soil moisture availability during this period. Conversely, in the spring and summer months, the situation reverses, with the mean monthly Q_E , reaching its zenith of close to 300 W m^{-2} at noon, outpacing the mean monthly Q_H , which reaches a maximum of approximately 220 W m^{-2} at noon. This shift is a consequence of elevated precipitation levels during this period, which enhances soil moisture availability in the Mantaro valley. Furthermore, the replenishment of nocturnal Q^N loss is notably more effective through Q_G than turbulent fluxes. This distinction becomes more pronounced in the winter months, where Q_E is almost negligible during the night, and the atmosphere exhibits stratification due to low surface temperatures and diminished soil moisture levels (Flores-Rojas et al., 2019a).

3 Instrumentation

3.1 Sensors

The Geophysical Institute of Peru implemented the Laboratory of Physics, Microphysics and Radiation (LAMAR) in 2015 at the HYGO. LAMAR has a set of varied instruments and sensors that can be used to measure several atmospheric properties with high temporal and spatial resolutions and to validate numerical physical



models in the Mantaro valley. All devices were installed in a 6-m high tower as a part of BSRN stations (Figure 2A). The set of radiation sensors contains a set of three pyranometers CMP10 (Kipp & Zonen), a pyrheliometer CHP1 (Kipp & Zonen) and two pyrgeometers CGR4 (Kipp & Zonen) (Figure 2B), to measure the hemispherical shortwave (SW) irradiance components and longwave (LW) irradiance incident and emitted by the surface, respectively. Two of the pyranometers were used to measure the SW global and diffuse irradiances incident at the surface, and the last one was used to measure the SW irradiance reflected by the surface. To measure the diffuse irradiance from the sky by blocking the direct solar irradiance we used a small black sphere mounted on an articulated, shading assembly in a two-axis automatic sun tracker 2AP (Kipp & Zonen). More details about these radiative sensors can be found in recent contributions (Flores-Rojas et al., 2019a; Ilores-Rojas et al., 2021). Figure 2C shows the heliograph from Campbell-Stokes installed at 1.5 m on the HYGO to measure sunshine hours and finally, Figure 2D, shows the location of LAMAR's instruments and sensors inside the HYGO.

4 Methodology

4.1 Database

In this study, we evaluate the primary atmospheric variables on the HYGO by analyzing measurements collected from a set of automatic sensors belonging to the surface weather station as illustrated in Figure 2D and the solar irradiance data by analyzing measurements from the BSRN station showed in Figures 2A, B. Both systems are operated by the Geophysical Institute of Peru (IGP). The details of these data sources are provided below:

1. Values of air temperature (°C), relative humidity (%), precipitation (mm min^{-1}) and water mixing ratio (g kg^{-1}) with 1 minute resolution carried out at the surface weather station

at 2 m height located on the HYGO between May 2017 and December 2022 (68 months and 2,100 days approximately).

2. Values of global, diffuse and direct solar irradiance (W m^{-2}) with 1 minute resolution carried out at the BSRN station at 6 m height located on the HYGO between May 2017 and December 2022 (68 months and 2,100 days approximately).

In meteorological measurement systems, the recording of data often encounters challenges. In the case of radiometers, measurement errors typically arise from several factors, including sensor misalignment or tilting, interference from nearby objects causing shadowing and reflections, and the accumulation of dust and moisture on the sensor dome (Bacher et al., 2013; Vuilleumier et al., 2014). Additionally, the behavior of solar radiation components is influenced by various factors such as cloudiness patterns, aerosol optical depth, surface albedo, cloud type, among others (Perez et al., 1990; Gueymard, 2005), making the development of universal models a complex task. For this work, we conducted distinct data quality checks to identify and rectify missing data, data points that clearly deviated from physical constraints, and extreme data outliers.

In cases where data were confirmed as 'erroneous' or 'missing,' the corresponding data fields were filled with a specific key sequence of numbers unique to the reporting location, serving as a clear indicator of the problematic observations. Any data associated with flagged 'bad' or 'missing' data was subsequently excluded from the dataset. Furthermore, a secondary filter was applied to eliminate hours featuring observations that violated fundamental physical principles or conservation laws. This included the removal of hours where reported values exhibited anomalies such as negative radiation values, diffuse fractions exceeding 1, beam radiation surpassing extraterrestrial beam radiation levels, and instances where the dew point temperature exceeded the dry bulb temperature (Reindl et al., 1990).

Additionally, we conducted a rigorous visual quality control process on the dataset, aiming to identify and rectify inconsistencies

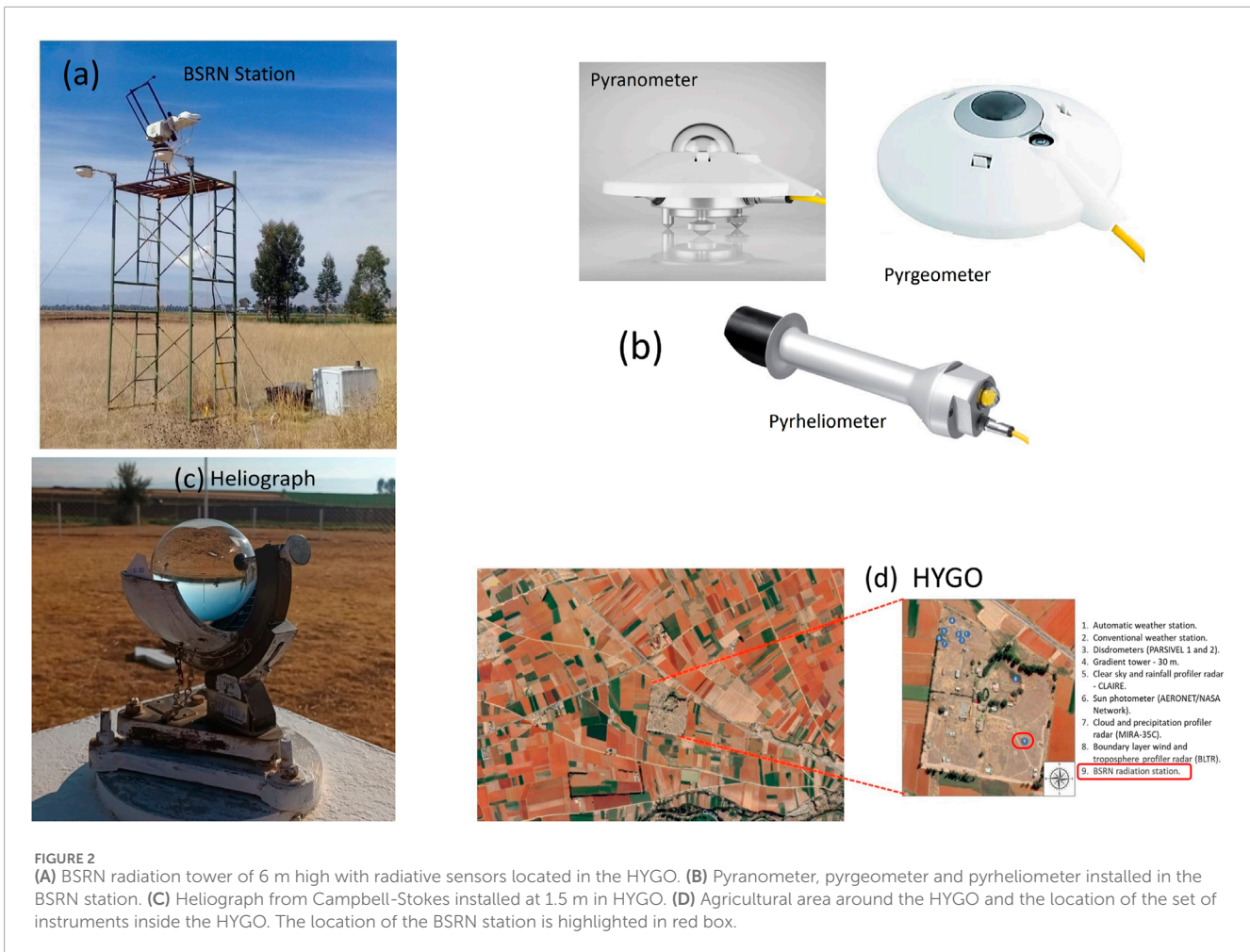


FIGURE 2

(A) BSRN radiation tower of 6 m high with radiative sensors located in the HYGO. (B) Pyranometer, pyrgeometer and pyrheliometer installed in the BSRN station. (C) Heliograph from Campbell-Stokes installed at 1.5 m in HYGO. (D) Agricultural area around the HYGO and the location of the set of instruments inside the HYGO. The location of the BSRN station is highlighted in red box.

and spikes that could be attributed to electronic malfunctions within the data acquisition system. Furthermore, we applied the methodology introduced by Younes et al. (2005) and Journee and Cedric (2010) to analyze the time series data. Data points were considered valid if they met specific criteria, including a solar elevation angle (α) greater than 2° , as well as satisfying the following ratios:

$$\frac{E_G}{E_T} < 1.2, \quad \frac{E_{DF}}{E_T} < 0.8, \quad \frac{E_{DR}}{E_T} < 1.0, \quad (1)$$

Here, E_T represents the extraterrestrial solar radiation incident on a horizontal surface. This value was estimated analytically according to Iqbal (1983), using a value for the solar constant set at 1367 W m^{-2} (Frohlich and Lean, 1998). These conditions (Equation 1) are suitable for stations that measure direct and diffuse components, independently Younes et al. (2005). A more lenient criterion, $E_G/E_T < 1.2$, led to the removal of 8.15% of the dataset, with no observable dependence on atmospheric turbidity or seasonality.

However, the most stringent criterion, $E_{DF}/E_T < 0.8$, resulted in the exclusion of 9.58% of the dataset, predominantly during the summer months (characterized by increased rainfall) (Marques Filho et al., 2016). Lastly, the criterion $E_{DR}/E_T < 1.0$ led to the exclusion of 7.89% of the dataset. Moreover, approximately 3.0% of the dataset was excluded based on the criterion of $\alpha > 2^\circ$. This primarily corresponded to measurements

taken during sunrise and sunset periods characterized by elevated atmospheric turbidity, notably during the winter and spring seasons.

Following rigorous data quality control procedures, we identified and selected data equivalent to 1850 days (44 400 h) to effectively capture the seasonal variations in solar irradiance across the region. This dataset encompasses approximately 88% of the entire observational period. Subsequently, comprehensive statistical analyses were conducted on various measurements, including those of E_G , E_{DF} and E_{DR} and other relevant meteorological variables.

The present study employs two key indexes to analyze atmospheric radiometric properties and develop empirical and correlation models: the clearness index (K_T), calculated as the ratio of E_G to E_T , and the diffuse fraction (K_D), expressed as the ratio of E_{DF} to E_G , as defined in Liu and Jordan (1960). Under clear sky conditions, a substantial portion of extraterrestrial radiation reaches the Earth's surface, resulting in E_G tending to E_T , K_T approaching 1 and K_D close to 0. Conversely, during cloudy conditions, E_G approaching to E_{DF} , leading to K_T nearing 0 and K_D approaching 1. The principal advantage of utilizing K_T and K_D lies in their ability to eliminate astronomical dependencies while preserving essential information concerning the influence of clouds, moisture levels, and aerosol concentrations on radiometric properties. This approach results in a more universally applicable description of these properties, enabling their use in regions with similar climatic characteristics.

4.2 Solar irradiance models

To develop the regression models of this section, the filtered dataset from May 2017 to December 2022 (1850 days or 44 400 h) as described in Section 4.1 was divided into two segments. Sixty percent (60%) of the total filtered dataset chosen randomly (1,110 days or 26 640 h), were used to construct the regression models, while the remaining forty percent (40%) of the total filtered dataset chosen randomly (740 days or 17 760 h) were reserved for rigorous statistical tests to evaluate model performance and robustness.

In early modeling efforts worldwide, the core focus was on linking daily horizontal global irradiation to bright sunshine duration. This phase involved creating regression equations using monthly-averaged data as the basis, providing foundational insights for solar energy prediction and utilization studies. The original [Angstrom \(1924\)](#) regression equation established a connection between monthly-averaged daily irradiation and irradiation on clear days. However, this approach presents challenges in precisely defining what constitutes a clear day. In response to this issue, several researchers ([Garg and Garg, 1985](#); [Turton, 1987](#)), have devised alternative relationships, exemplified by the subsequent equation:

$$\frac{\overline{E_G}}{\overline{E_T}} = \left[a + b \left(\frac{n}{N} \right) \right] \tag{2}$$

where $\overline{E_G}$ and $\overline{E_T}$ are the monthly-averaged daily terrestrial and extraterrestrial global irradiance on a horizontal surface, n is the average daily hours of bright sunshine and N is the day length, obtained by:

$$\omega_s = \cos^{-1}(-\tan \text{LAT} \tan \text{DEC}), \quad N = (2\omega_s/15) \tag{3}$$

where ω_s is expressed in degrees, LAT is the latitude of the HYGO (12°S) and DEC is the solar declination angle. The ratio n/N is known as fractional possible sunshine. The extraterrestrial irradiation, E may be calculated analytically according to [Munner \(2004a\)](#). Moreover, the initial development of a regression model between monthly-averaged values of diffuse and global irradiances can be attributed to [Liu and Jordan \(1960\)](#), presented as $\overline{E_D}/\overline{E_G}$ in relation to $\overline{K_T} = \overline{E_G}/\overline{E_T}$, where $\overline{E_D}$ represents the monthly-average daily diffuse radiation incident on a horizontal surface. This pioneering approach has garnered international attention, with numerous researchers confirming its applicability worldwide. However, it has been noted that observed data often deviates from predictions made using the Liu–Jordan model, raising questions regarding its universality and generality. The equation to estimate the monthly-averaged diffuse irradiance can be parameterized by:

$$\frac{\overline{E_D}}{\overline{E_G}} = a - b \overline{K_T} \tag{4}$$

Several values for the coefficients a and b have been proposed worldwide. For instance, [Hawas and Muneer \(1984\)](#) obtained $a = 1.35$ and $b = 1.61$ for the India subcontinent and [Page \(1977\)](#) obtained $a = 1.0$ and $b = 1.13$ for eight United Kingdom and nine worldwide locations.

On the other hand, [Cowley \(1978\)](#) derived a series of linear regression equations linking daily global irradiance to the duration of bright sunshine at ten stations across Great Britain. These

equations offer a valuable means to estimate daily incident radiation, a more granular measure, as opposed to monthly-averaged values. Cowley’s equation is given as:

$$\frac{E_G^d}{E_T^d} = \left\{ d \left[a + b \left(\frac{n}{N} \right) \right] + (1 - d) a' \right\} \tag{5}$$

where E_G^d and E_T^d are the daily global and extraterrestrial irradiances, respectively. The ratio n/N is the daily sunshine. The parameter d satisfies this condition $d = 0$ if $n = 0$, otherwise $d = 1$ if $n > 0$, and a' is equal to the average ratio of E_G^d/E_T^d for overcasts days. On the other hand, in the seminal study by [Liu and Jordan \(1960\)](#), they initially formulated a regression equation connecting the diffuse fraction of daily global irradiance ($K_D = E_D^d/E_G^d$), referred to as the diffuse ratio with the ratio of daily global to extraterrestrial irradiation (K_T) referred to as clearness index. Several contributions have used a third degree polynomial to estimate the diffuse ratio ([Le Baron and Dirmhirn, 1983](#); [Smietana et al., 1984](#); [Saluja et al., 1988](#); [Munner, 2004b](#)), which can be expressed as:

$$\begin{aligned} E_D^d/E_G^d &= a + b K_T - c K_T^2 + d K_T^3, \quad K_T > 0.2 \\ E_D^d/E_G^d &= 0.98, \quad K_T < 0.2 \end{aligned} \tag{6}$$

In general, the recommended coefficients of a global model for the diffuse ratio are: $a = 0.962$, $b = 0.779$, $c = 4.375$ and $d = 2.716$ according to [Munner \(2004a\)](#). Furthermore, the use of hourly irradiation data significantly enhances the precision of modeling solar energy processes. However, considering that daily irradiation measurements are more widely available across various sites compared to their hourly counterparts, it is imperative to explore the correlation between these two temporal scales. Many meteorological stations routinely report their data in the form of monthly-averaged values of daily global irradiance, making it a crucial point of investigation.

The pioneering work in this field is attributed to [Whillier \(1956\)](#), whose research laid the foundation. Building upon Whillier’s findings, [Liu and Jordan \(1960\)](#) extended and refined the framework. They developed a series of regression curves, which take into account the impact of temporal displacement from solar noon and day length on the hourly-to-daily global irradiation ratio (r_G). [Collares-Pereira and Rabl \(1979\)](#) subsequently reaffirmed the accuracy of Liu and Jordan’s plots. Employing a least-squares fitting approach, they further refined the models, yielding:

$$r_G = \frac{\pi}{24} (a' + b' \cos \omega) \frac{\cos \omega - \cos \omega_s}{\sin \omega_s - \omega_s \cos \omega_s} \tag{7}$$

where ω represents the solar hour angle, 15° for each hour displaced from the true solar noon, ω_s is given by the [Equation 3](#). The coefficients a' and b' are given by:

$$\begin{aligned} a' &= r + s \sin (\omega_s - 1.047) \\ b' &= p + q \sin (\omega_s - 1.047) \end{aligned} \tag{8}$$

The coefficients are given by: $r = 0.409$, $s = 0.5016$, $p = 0.6609$ $q = 0.4767$. Another authors have used similar equations with different coefficients ([Saluja and Robertson, 1983](#); [Hawas and Muneer, 1984](#)). In this work, we find the best coefficients r , s , p , and q , by fitting the [Equation 7](#) to the observed global irradiance data. Moreover, to calculate long-term hourly diffuse irradiation averages, one can

derive them from monthly-average daily diffuse irradiation values, provided that the hourly-to-daily diffuse irradiation ratio, denoted as r_D is known. For the present work, we used a generalized equation based on the formula introduced by Liu and Jordan (1960) but with coefficients similar to Equation 7, as:

$$r_D = \frac{\pi}{24} (c' + d' \cos \omega) \frac{\cos \omega - \cos \omega_s}{\sin \omega_s - \omega_s \cos \omega_s} \quad (9)$$

where ω is the same that the Equation 7 and the coefficients c' and d' are:

$$\begin{aligned} c' &= t + u \sin(\omega_s - 1.047) \\ d' &= v + w \sin(\omega_s - 1.047) \end{aligned} \quad (10)$$

Similar to the previous case of the Equation 7, we find the best coefficients t , u , v , and w , by fitting the Equation 9 to the observed diffuse irradiance data.

4.3 Correlation models between K_D^h and K_T^h

For the present study, we employed a diverse range of logistic functions to establish correlations between the hourly diffuse fraction (K_D^h) and the hourly clearness index (K_T^h). These encompassed sigmoid logistic functions (Boland and Ridley, 2008; Marques Filho et al., 2016), a fourth-degree polynomial function (Oliveira et al., 2002a), and a three-degree polynomial function (Jacovides et al., 2006). As mentioned previously, to develop the regression models in this section, the filtered dataset from May 2017 to December 2022 (1850 days or 44,400 h), as described in Section 4.1, was divided into two segments. Sixty percent (60%) of the total filtered dataset, chosen randomly (1,110 days or 26,640 h), was used to construct the regression models. The remaining forty percent (40%), chosen randomly (740 days or 17,760 h), was reserved for rigorous statistical tests to evaluate model performance and robustness.

4.4 Statistical indicators

To evaluate the performance of different solar irradiance models, we used the traditional statistical indicators: R-squared (R^2) which indicates the percentage of the variance in the dependent variable that the independent variables explain collectively, R^2 measures the strength of the relationship between your model and the dependent variable on a convenient 0% – 100% scale. In addition, the mean squared error (MSE) assesses the average squared difference between the observed and predicted values. When a model exhibits zero error, its MSE becomes zero as well. As the model's error increases, so does the MSE value.

On the other hand, in the case of correlation models involving K_D^h and K_T^h , we employed the Akaike's Information Criterion (AIC) (Marques Filho et al., 2016). This criterion serves as a means to assess the performance of various correlation models, and it is defined as follows:

$$AIC = \ln \left(\frac{\sum (y_i - \mu_i)^2}{n} \right) + \frac{2k}{n} \quad (11)$$

In this equation, y_i represents the observed data, μ_i signifies the modeled data, n stands for the sample size, and k denotes the number of model parameters (Motulski and Christopoulos, 2003). The second term on the right side of this equation accounts for a penalty based on the number of parameters within the model. However, to gauge a model's performance in comparison to others, it becomes essential to compute the difference of AIC:

$$\Delta_i AIC = AIC_i - AIC_{min} \quad (12)$$

In this context, AIC_i represents the AIC value corresponding to model i , and AIC_{min} denotes the minimum AIC value calculated among various models. This transformation is designed to ensure that the top-performing model registers a $\Delta_i AIC$ of 0, while all other models exhibit positive values (Burnham and Anderson, 2004).

5 Results

5.1 Atmospheric variables

In this work, the main climate features of the west region of the Mantaro valley are assessed based on measurements carried at the HYGO conventional meteorological station and the short-term meteorological variables from an automatic station of the Geophysical Institute of Peru (IGP) at the HYGO, as described below:

1. Three times a day values of air temperature (T), relative humidity (RH), accumulate precipitation and cloudiness carried out at the surface weather station located in the HYGO from January 1981 to December 2020 (40-year climate normal) (Giráldez et al., 2020).
2. One-minute average values of T, RH and precipitation measured from May 2017 to December 2022 at IGP platform in the HYGO. More information about the instruments installed in the automatic station of HYGO can be found in a recent contribution (Flores-Rojas et al., 2021).

According to Köppen-Geiger (Peel et al., 2007) and considering climatological observations of atmospheric variables carried out on the HYGO (Figure 3) is classified as Cwb. In consequence, the MV can be considered as temperate with dry winter (June-August) and warm summer (December-February). The criteria that define this climate zone are: mean temperature of the hottest month higher than 10°C, for the HYGO is close to 14°C, the mean temperature of the coldest month is between 0°C and 18°C, for the HYGO is close to 10°C (Figure 3A). Also, the number of months where the mean temperature is above 10 is greater than 4. Moreover, the annual amplitude of the monthly average air temperature ($T_{(1981-2020)}$) presents minimums in February with values around 12°C and maximums in July with values around 20°C (Figure 3A).

Another important criteria are: the precipitation of the driest month in summer is close to 90 mm month⁻¹, the precipitation of the driest month in winter is close to 6 mm month⁻¹, the precipitation of the wettest month in summer is close to 130 mm month⁻¹ and the precipitation of the wettest month in winter is close to 12 mm month⁻¹. The accumulate precipitation in the summer is equal to 340 mm (Dec-Feb), with maximum of

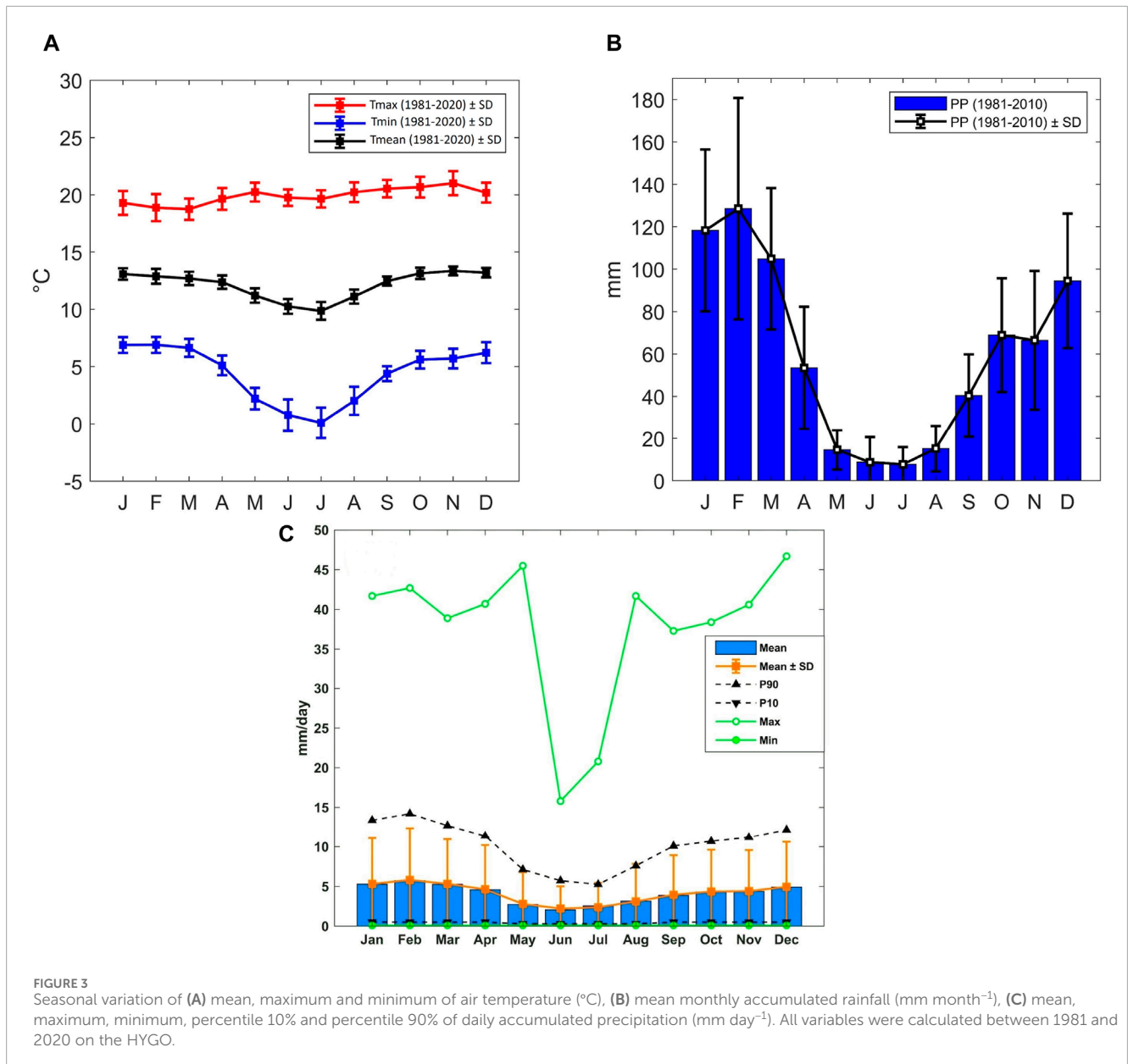


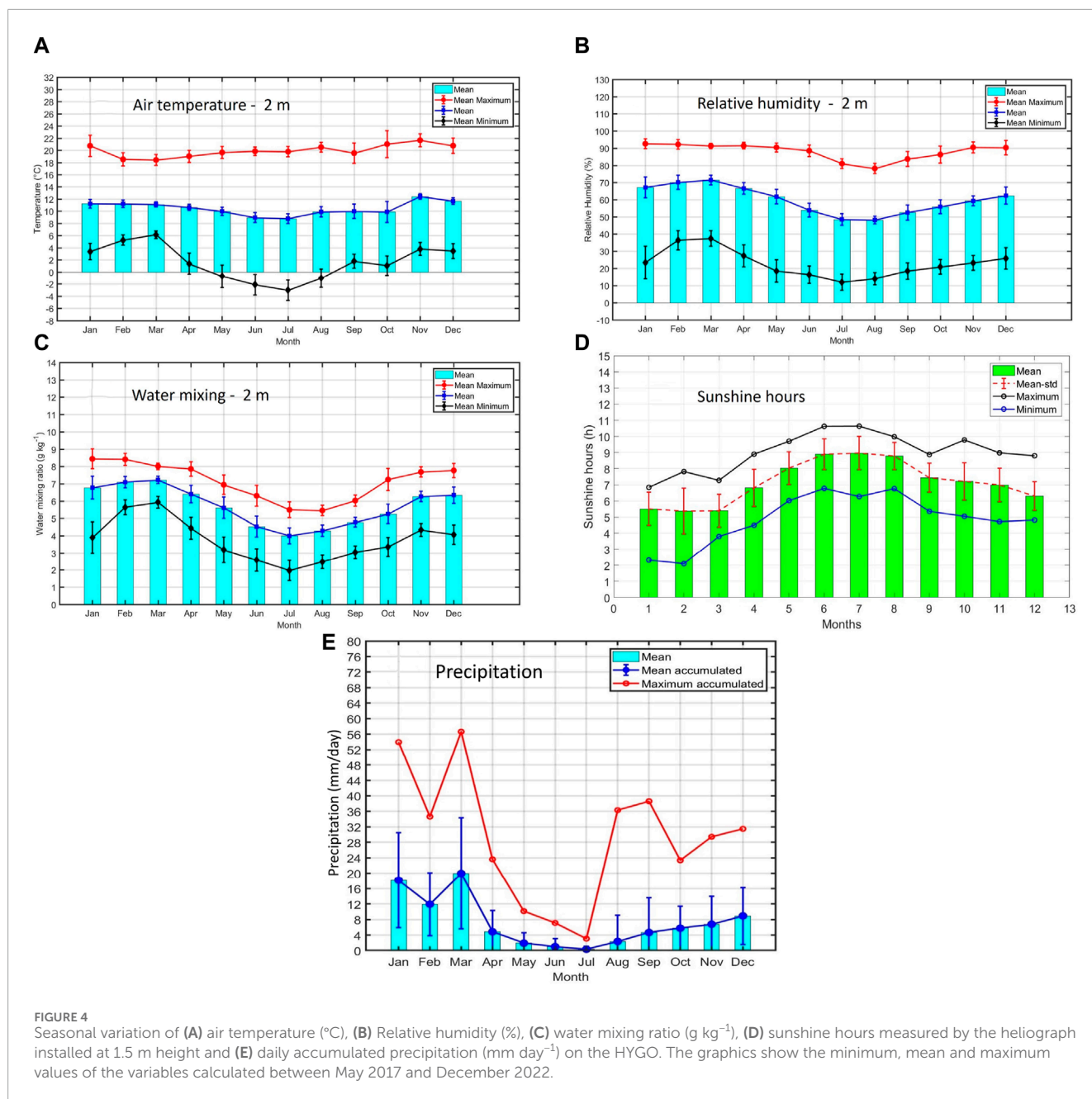
FIGURE 3 Seasonal variation of (A) mean, maximum and minimum of air temperature ($^{\circ}\text{C}$), (B) mean monthly accumulated rainfall (mm month^{-1}), (C) mean, maximum, minimum, percentile 10% and percentile 90% of daily accumulated precipitation (mm day^{-1}). All variables were calculated between 1981 and 2020 on the HYGO.

130 mm in February. In the winter (Jun-Aug), the accumulated precipitation is 28 mm (Jun-Aug), with minimum of 6 mm in July (Figure 3B). Moreover, the maximum daily accumulated precipitation is observed during May and December with values around 45 mm day^{-1} and the minimum during June with values close to 15 mm day^{-1} (Figure 3C).

All instances of intense rainfall events on the HYGO exhibited discernible thermal meso-scale circulations linked to the South American Low-Level Jet (SALLJ). These circulations facilitated the transportation of moisture fluxes originating from both the Amazon basin in the east—traversing the passes with gentle slopes along the Andes—and the Pacific Ocean in the west. This atmospheric phenomenon unfolded in the hours leading up to the occurrence of intense rainfall events within the MV. Furthermore, our investigations revealed two primary regions on the eastern side of the Andes where moisture influxes penetrated

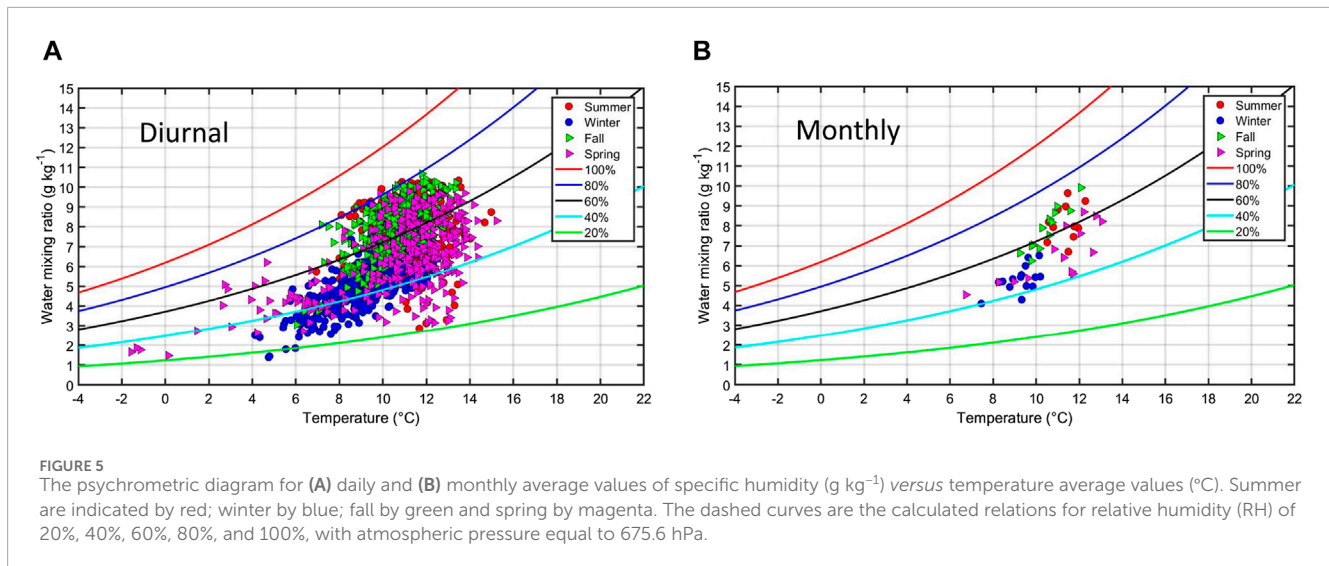
the central Andes: one situated in the north-western region (Blue Cordillera) and the other in the south-eastern region of the Mantaro Basin.

On the western side of the Andes, several small passes with gradual slopes served as conduits for moisture fluxes originating from the Pacific Ocean (Flores-Rojas et al., 2019b). The impact of these meso-scale circulations became particularly pronounced during intense rainfall events occurring between 14 LT and 23 LT. The trajectory of these moisture flows into specific regions within the MV hinged on their interaction with circulations at medium and high atmospheric levels. Within this framework, we identified two distinct sets of atmospheric circulations that gave rise to severe rainfall events above the HYGO: the EC (East Circulation) and WC (West Circulation) events. These were characterized by the prevailing atmospheric circulations at high and medium levels, respectively (Flores-Rojas et al., 2020).



To validate the micro-climate data recorded at the HYGO automatic station (2017–2022), we compare seasonal variations in air temperature and daily accumulated precipitation with a 40-year climate normal (1981–2020) from the conventional weather station of the HYGO. This analysis ensures the representativeness and reliability of the observed micro-climate trends. In general, comparatively to the climate normal, the observations in the HYGO automatic station indicate that the climate on the HYGO during the period of 2017–2022 are very similar to the climatology values of temperature (Figure 3A), with mean maximums close to 22°C in November and mean minimums close to -3°C in July, with minimum diurnal thermal amplitude close to 12°C in March and maximum close to 23°C in July (Figure 4A).

Furthermore, Figure 4E illustrates the seasonal dynamics of daily accumulated precipitation from 2017 to 2022, exhibiting a pattern consistent with the 40-year precipitation climate normal depicted in Figure 3C. During this period, the maximum daily accumulated precipitation peaks in March, reaching approximately 56 mm day⁻¹, while the minimum values, around 4 mm day⁻¹, are observed in July. Additionally, Figure 4B portrays the seasonal fluctuations in relative humidity (RH) from 2017 to 2022. Notably, the smallest amplitude of RH occurs in March, with values close to 52%, while the maximum amplitude is observed in January, reaching approximately 68%. The seasonal variation of water vapor mixing ratio between 2017 and 2022 is depicted in Figure 4C. Mean maximum values are observed during in January and February



with values close to 8.5 g kg^{-1} and minimum values around to 2 g kg^{-1} in July.

Finally, Figure 4C shows the seasonal variation of sunshine hours from 2017 to 2022 registered by the Heliograph installed on the HYGO (Figure 2C). Maximum values of sunshine hours are observed in June and July with values close to 10.5. It is important to note that October also has high maximum sunshine hours around to 10. This set of data is important because initial modeling work carried out around the world was involved in relating daily horizontal global irradiation to duration of bright sunshine hours.

An alternative approach to assess the representativeness of measurements obtained from the HYGO automatic station involves utilizing the psychrometric diagram for characterizing the seasonal climate conditions in the area (Gaffen and Ross, 1999). Figures 5A, B illustrate the psychrometric diagram for daily and monthly average values of specific humidity (q) (g kg^{-1}) and temperature (T) ($^{\circ}\text{C}$), respectively. Both figures reveal a moderate correlation between specific humidity (q) and temperature (T), with values reaching approximately 60% for mean diurnal averages and 75% for mean monthly averages. The seasonal average daily values (Figure 5A) of q range from 1.5 g kg^{-1} on a few spring days to 11 g kg^{-1} on certain days in fall and summer. The colored lines in the figure represent the values of q as a function of T for different relative humidity (RH) levels, with atmospheric pressure set to 675.6 hPa (mean pressure at HYGO).

Throughout all seasons, the range of daily average RH values fluctuates between 20% and 90%. The increased dispersion in the monthly average values recorded at the HYGO automatic station, particularly notable during the summer and spring, appears to be linked to climatic variability. This variability is indicative of warmer and drier conditions experienced during these seasons in recent years. Additionally, the seasonal average monthly values (Figure 5B) of q vary between 4 g kg^{-1} in winter and 10 g kg^{-1} in fall and summer. Similar to the daily values, the colored lines in the figure depict the relationship between q and T for different RH levels, considering the atmospheric pressure of 675.6 hPa (mean pressure at HYGO). Monthly average RH values consistently fall within the range of 40% and 75%, as demonstrated in Figure 4B.

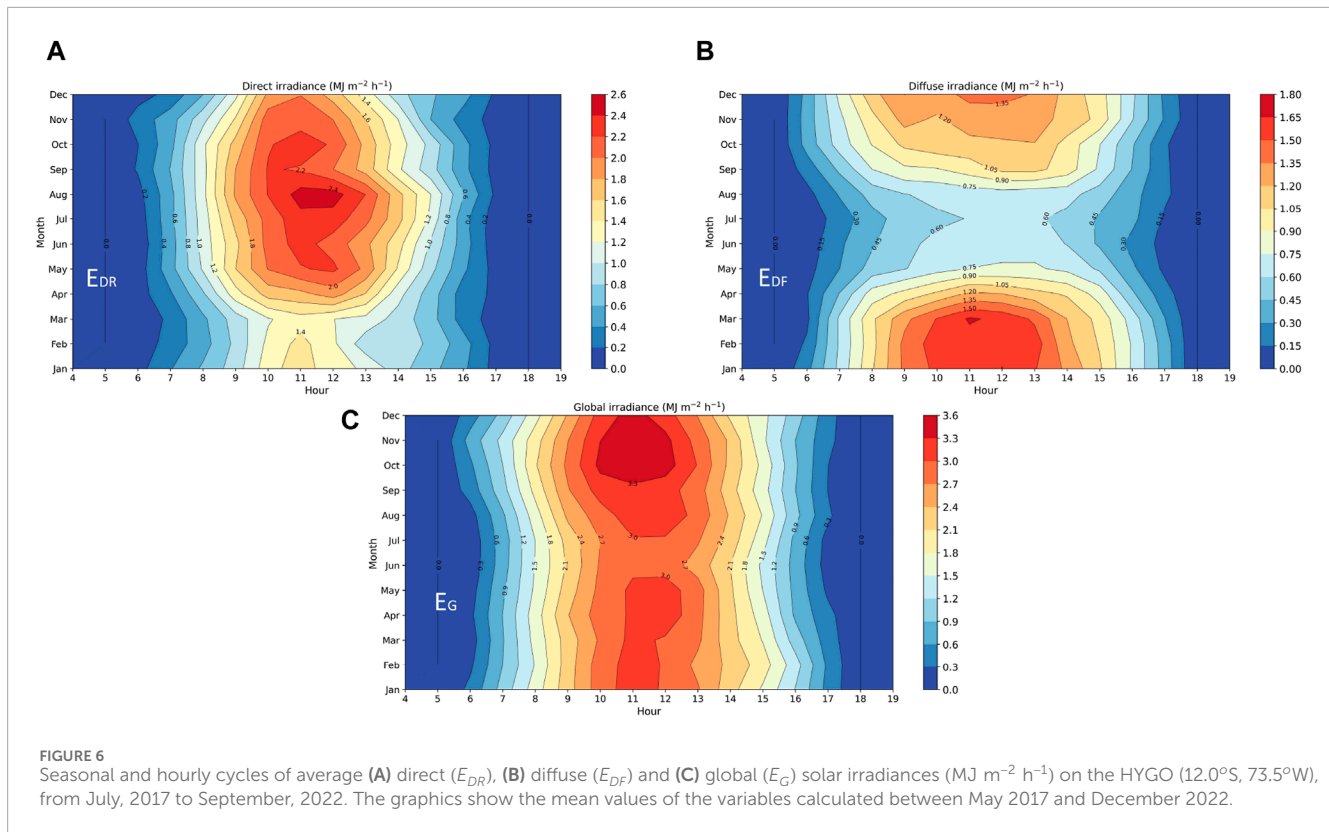
Hence, based on the climate analysis conducted herein, it can be inferred that the radiation measurements recorded between 2017 and 2022 on the HYGO automatic station might be influenced by the fact that the HYGO region experienced cooler and drier conditions during this period compared to the climatological norm. Despite these variations, as detailed in Section 5.2, it will be demonstrated that the mean behavior of E_G at the surface aligns with estimates derived from normal values of sunshine hours. This alignment suggests that it can be deemed representative of the climate in the MV region. On the other hand, the E_{DF} and E_{DR} components of solar radiation, measured at the HYGO automatic station, appear to exhibit a greater sensitivity to local climate and land-use characteristics.

5.2 Irradiance variables

In this section, we delineate the time-integrated values of surface solar radiation components denoted by $E_{X'}^Y$, expressed in megajoules per unit area per hour ($\text{MJ m}^2 \text{ h}^{-1}$). The subscripts X (T, G, DF, and DR) represent extraterrestrial, global, diffuse, and direct solar radiation, respectively. All irradiance variables E_{DR} , E_{DF} , E_G components observed at the surface. The superscripts Y (h and d) signify time intervals for integration, with “h” representing 1 hour and “d” representing 1 day.

5.2.1 Seasonal variation of hourly values

The seasonal fluctuation in the diurnal evolution of E_{DR}^h (Figure 6A) is derived from the matrix of monthly average E_{DR}^h values, which are interpolated using the cubic spline method (Boor, 2001). The monthly average of E_{DR}^h at noon reaches a peak close to $2.5 \text{ MJ m}^2 \text{ h}^{-1}$ during winter (July) and dipping to a minimum close to $1.2 \text{ MJ m}^2 \text{ h}^{-1}$ in summer (February). Moreover, the monthly average of E_{DF}^h (Figure 6B) at noon reaches a peak around $1.80 \text{ MJ m}^2 \text{ h}^{-1}$ during summer (February) and dipping to a minimum around $0.45 \text{ MJ m}^2 \text{ h}^{-1}$ in winter (July). Notably, the longest and shortest duration of sunshine hours occur in July (9 h) and February (5.5 h), respectively.



On the contrary, the monthly average of E_G^h (Figure 6C) at noon reaches a peak around $3.6 \text{ MJ m}^{-2} \text{h}^{-1}$ during spring (October) and dipping to a minimum close to $2.7 \text{ MJ m}^{-2} \text{h}^{-1}$ in winter (July). The highest E_G^h in spring months is associated to a combination of astronomical factor, cloudiness and aerosol concentration patterns observed during 2017–2022 in the HYGO. During this period, the daily accumulated precipitation reach maximum and mean values around 24 mm day^{-1} and 5 mm day^{-1} , respectively. The maximum value is below the climate normal in October with maximums close to 37 mm day^{-1} and the mean value is close to the climate mean value around 4 mm day^{-1} . In addition, the sunshine hours during October reach a maximum close to 10 h (Figure 4). The combination of these factors indicates that the reduction in the precipitation and the moderate presence of aerosols seems to be associated to the reduction in the cloud cover that favored large values of E_G^h .

The diurnal evolution of monthly average of E_T^h , E_G^h , E_{DF}^h and E_{DR}^h , during summer, fall, winter and spring months are shown in Figures 7A–D, respectively. In addition, Table 1 shows the specific values for the diurnal cycle of these irradiance variables. All components of solar irradiance exhibit a clearly defined diurnal cycle, reaching their maximum intensity at noon. The minimal standard error of the mean, denoted by the small vertical bars, signifies that the monthly average values of solar radiation components recorded at the surface within the HYGO accurately reflect the mean conditions observed in the MV.

During summer at noon, E_G^h ($3.11 \pm 0.16 \text{ MJ m}^{-2} \text{h}^{-1}$) constitutes 64.4% of E_T^h ($4.83 \pm 0.14 \text{ MJ m}^{-2} \text{h}^{-1}$). Additionally, E_{DF}^h ($1.67 \pm 0.22 \text{ MJ m}^{-2} \text{h}^{-1}$) and E_{DR}^h ($1.37 \pm 0.21 \text{ MJ m}^{-2} \text{h}^{-1}$) represent 53.7% and 44.10% of E_G^h ($3.11 \pm 0.16 \text{ MJ m}^{-2} \text{h}^{-1}$), respectively. In contrast, during winter at noon, E_G^h ($3.08 \pm 0.14 \text{ MJ m}^{-2} \text{h}^{-1}$)

accounts for 78.2% of E_T^h ($3.94 \pm 0.11 \text{ MJ m}^{-2} \text{h}^{-1}$). Moreover, E_{DF}^h ($0.64 \pm 0.16 \text{ MJ m}^{-2} \text{h}^{-1}$) and E_{DR}^h ($2.27 \pm 0.19 \text{ MJ m}^{-2} \text{h}^{-1}$) represent 20.8% and 73.7% of E_G^h , respectively.

On the other hand, during fall at noon, E_G^h ($3.02 \pm 0.18 \text{ MJ m}^{-2} \text{h}^{-1}$) constitutes 69.7% of E_T^h ($4.33 \pm 0.14 \text{ MJ m}^{-2} \text{h}^{-1}$). Furthermore, E_{DF}^h ($1.18 \pm 0.17 \text{ MJ m}^{-2} \text{h}^{-1}$) and E_{DR}^h ($1.65 \pm 0.23 \text{ MJ m}^{-2} \text{h}^{-1}$) represent 39.1% and 54.6% of E_G^h , respectively. Finally, it is noteworthy that during spring at noon, E_G^h ($3.32 \pm 0.22 \text{ MJ m}^{-2} \text{h}^{-1}$) surpasses the mean values in summer, constituting 70.0% of E_T^h ($4.74 \pm 0.17 \text{ MJ m}^{-2} \text{h}^{-1}$). Additionally, E_{DF}^h ($1.32 \pm 0.24 \text{ MJ m}^{-2} \text{h}^{-1}$) and E_{DR}^h ($1.92 \pm 0.27 \text{ MJ m}^{-2} \text{h}^{-1}$) represent 39.8% and 57.8% of E_G^h , respectively.

It is important to highlight that for all seasons the sum of E_{DF}^h and E_{DR}^h do not contribute 100% to the total E_G^h . We consider that these small differences are caused by the filters showed in Section 4.1 that removes several data of E_{DF}^h and E_{DR}^h mainly in hours close to noon, caused by fails of the sun-tracker 2AP (Kipp & Zonen) that move the pyrhemeter CHP1 (Kipp & Zonen) to measure E_{DR}^h and the small black sphere to measure E_{DF}^h . These problems are more evident during winter and fall seasons and will be corrected by the acquisition of a new sun-tracker.

The examination of K_T and K_D provides a more comprehensive insight into the diurnal pattern of atmospheric transmittance, as it eliminates the influence of astronomical factors on E_T , E_G , and E_{DF} . Consequently, K_T and K_D emerge as crucial indicators for discerning the scattering and absorption processes facilitated by the presence of clouds and aerosol loads in the atmosphere. The diurnal evolution of K_T^h shows a maximum close to 0.64 ± 0.04 at noon during summer (Figure 8A), around 0.71 ± 0.06 at 13 LT during fall (Figure 8B), close to 0.78 ± 0.04 at noon during winter

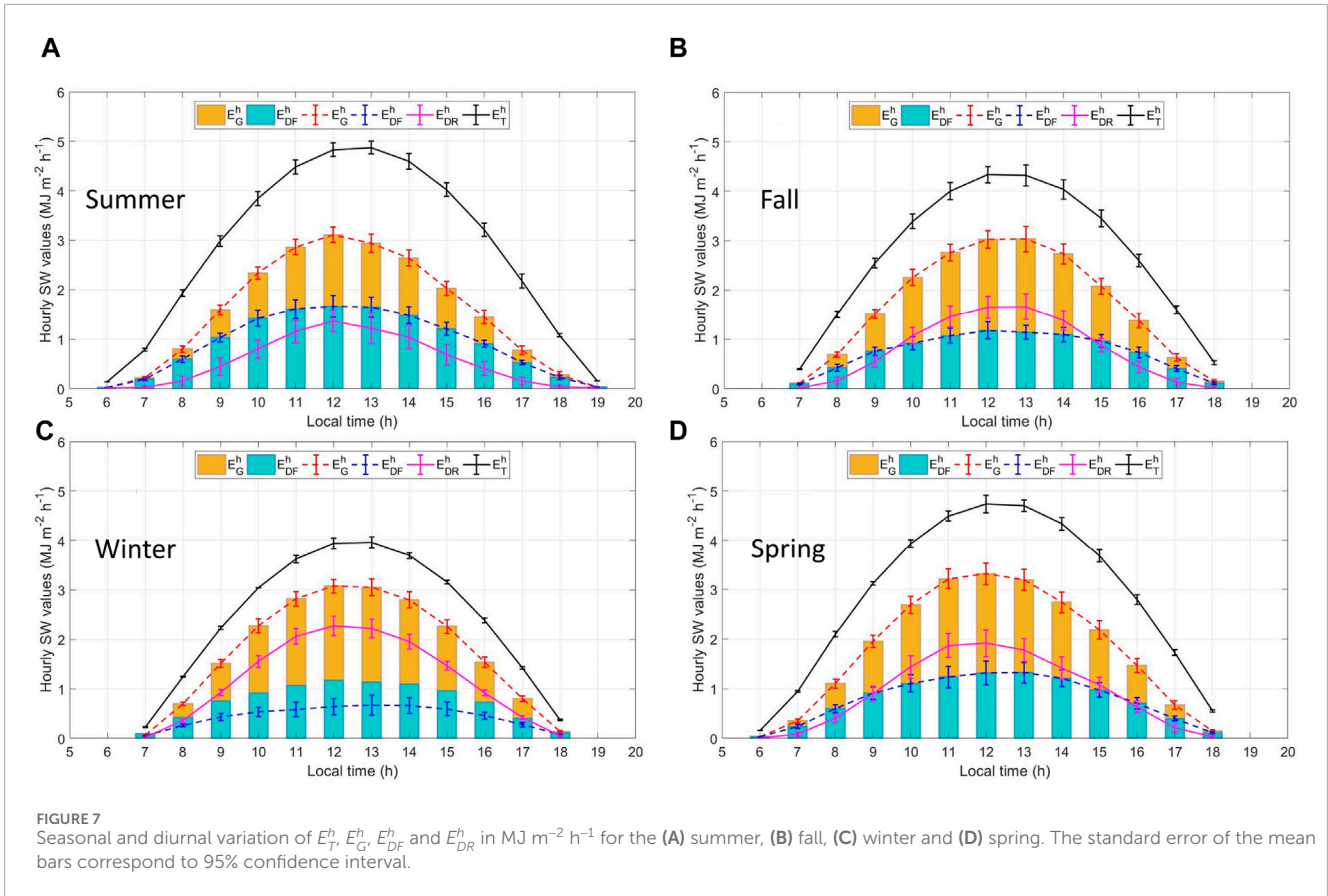


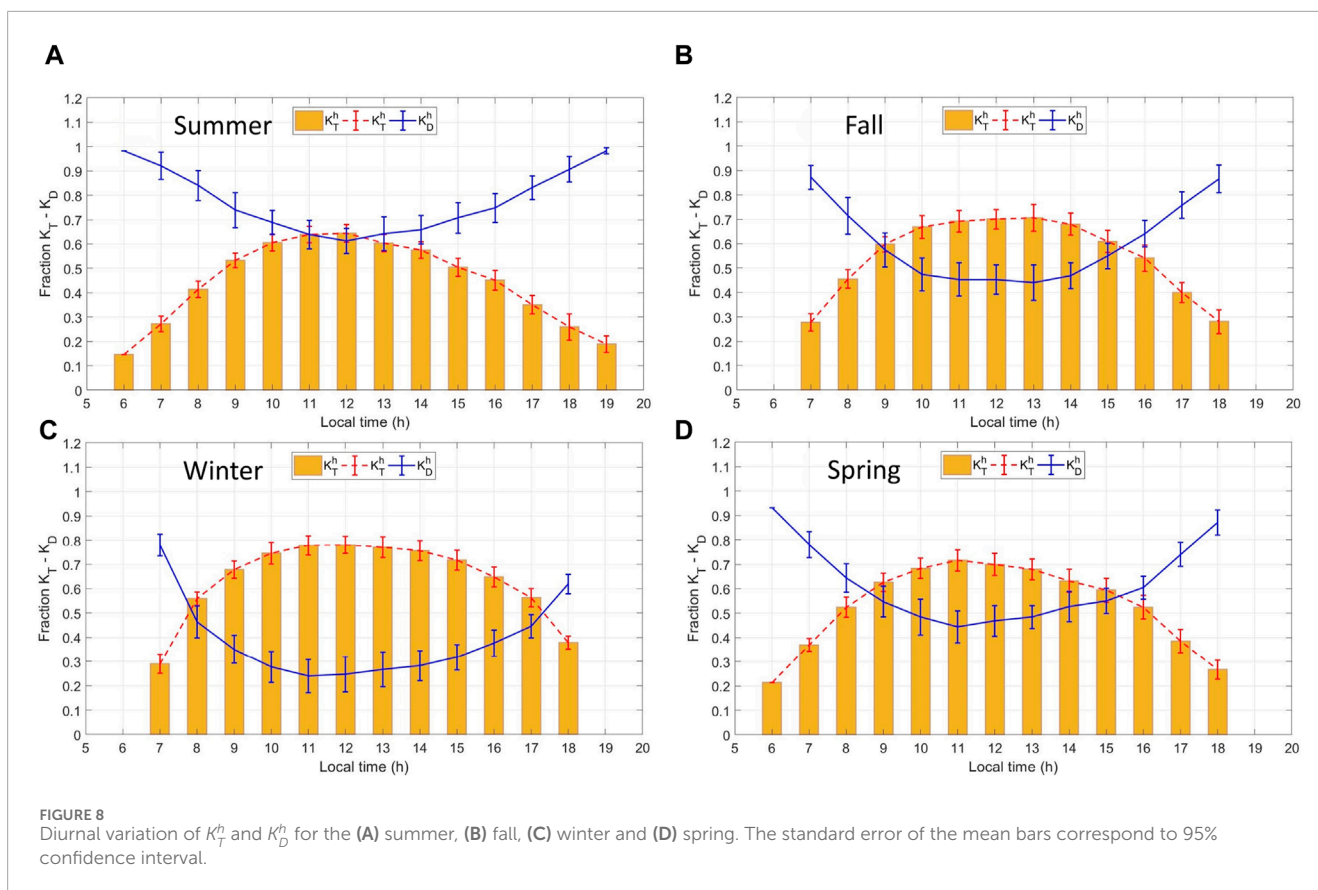
TABLE 1 Seasonally average hourly values of solar irradiance components: E_T^h , E_G^h , E_{DF}^h and E_{DR}^h , clearness index (K_T) and diffuse fraction (K_D) observed in the HYGO. The hourly values correspond to noontime (12 LT).

Irradiances ($\text{MJ m}^{-2} \text{h}^{-1}$)	Summer	Fall	Winter	Spring
E_T	4.83±0.14	4.33±0.16	3.94±0.11	4.74±0.17
E_G	3.11±0.16	3.02±0.18	3.08±0.14	3.32±0.22
E_{DF}	1.67±0.22	1.18±0.17	0.64±0.16	1.32±0.24
E_{DR}	1.37±0.21	1.65±0.23	2.27±0.19	1.92±0.27
Indexes	Summer	Fall	Winter	Spring
K_T	0.64±0.04	0.70±0.04	0.78±0.04	0.70±0.05
K_D	0.61±0.05	0.45±0.06	0.25±0.07	0.47±0.06

(Figure 8C) and around 0.72 ± 0.04 at 11 LT in spring (Figure 8D). In general, K_D^h has an inverse behavior in comparison with K_T^h . The diurnal evolution of K_D^h presents maximum values at noon also during summer close to 0.61 ± 0.05 and minimum during winter around 0.25 ± 0.07 . The amplitude of seasonally average values between K_T^h and K_D^h for the HYGO at noontime reach its minimum value in summer (0.03) and its maximum in winter (0.53) with intermediate values during fall (0.25) and spring (0.23) (Table 1).

5.2.2 Seasonal variation of daily values

The seasonal variation of monthly average daily values of the solar radiation components at the surface of the HYGO is presented in Figure 9A; Table 2. The highest values of E_G^d are observed in October (spring) around $24.14 \pm 2.10 \text{ MJ m}^{-2} \text{ day}^{-1}$ and the lowest values of E_G^d are observed in March (autumn) around $19.50 \pm 2.15 \text{ MJ m}^{-2} \text{ day}^{-1}$. Moreover, the highest values of E_{DR}^d are observed during August (winter) around $14.97 \pm 1.82 \text{ MJ m}^{-2} \text{ day}^{-1}$ but also are



observed high values of E_{DR}^d in September and October (spring) probably partially associated with high values of aerosol optical depth at 440 nm occurring during these months (Figure 9C). The lowest values of E_{DR}^d are observed during March (autumn) with values close to $6.59 \pm 1.89 \text{ MJ m}^{-2} \text{ day}^{-1}$. On the contrary, the highest values of E_{DF}^d are observed during January (summer), around $13.03 \pm 1.91 \text{ MJ m}^{-2} \text{ day}^{-1}$ and the lowest values are observed during July (winter) around $4.57 \pm 1.0 \text{ MJ m}^{-2} \text{ day}^{-1}$. This behavior of E_{DF}^d can be explained by the strongly seasonal variation of clouds and precipitation on the HYGO, previously analyzed (Figure 4E).

Furthermore, the seasonal evolution of K_T^d shows maximums close to 0.73 ± 0.06 in June and July (winter) and minimums around 0.54 ± 0.04 during January and February (summer). In general, the seasonal evolution of K_D^d has an inverse behavior in comparison with K_T^d with maximums in February (summer) close to 0.66 ± 0.08 and minimums during July (winter) with values around 0.24 ± 0.10 (Table 2). The amplitude of monthly average values between K_T^d and K_D^d for the HYGO reach its minimum value during March (0.05) and November (0.02) and reach maximum values in July (0.48) (Figure 9B).

To elucidate the seasonal variations in the average daily values of solar irradiance components (E_G^d , E_{DF}^d and E_{DR}^d), Figure 10 present the monthly mean values of aerosol volumetric size distributions. These distributions are derived from measurements taken with a CIMEL CE-318T sun photometer, part of the AERONET network (Holben et al., 1998; 2001). The data exhibit a generally bimodal behavior in the monthly mean size distributions, with a predominance of the coarse mode, as shown by the average

size distribution curve for the analyzed period (dashed line in all graphs). This bimodal pattern is also evident in the seasonal mean values (dotted lines), where larger aerosols dominate in all seasons except spring (Figure 10D). Specifically, coarse-mode aerosols are predominant in summer (Figure 10A), fall (Figure 10B), and winter (Figure 10C). These coarse-mode aerosols, with average radii around $5.0613 \mu\text{m}$, account for 56.3% of the cases and are primarily associated with marine and desert sources, with lesser contributions from continental aerosols. In contrast, fine-mode aerosols, with average radii around $0.1482 \mu\text{m}$ (43.7%), are mainly produced by the incomplete combustion of fossil fuels and biomass burning (Estevan et al., 2019).

During the spring season, there is a clear predominance of fine-mode aerosols, as illustrated in Figure 10D. This trend is evident in the seasonal mean (dotted line) and the monthly mean values, particularly in September and November. In September, the fine mode dominates, primarily due to aerosols generated by biomass burning in the Peruvian Amazon, which is associated with high Aerosol Optical Depth (AOD) values measured by the sun photometer at HYGO. Previous studies indicate that starting in July, AOD values rise due to biomass burning aerosols, peaking in September (Estevan et al., 2019). This increase aligns with the predominance of fine-mode aerosols in August (Figure 10C) and throughout the spring months (Figure 10D).

In an atmosphere with aerosols, more scattered energy reaches the ground due to increased forward scattering (Iqbal, 1983). During spring, the pronounced presence of both fine-mode (0.1482 m) and coarse-mode (5.0613 m) aerosols, combined with longer daily

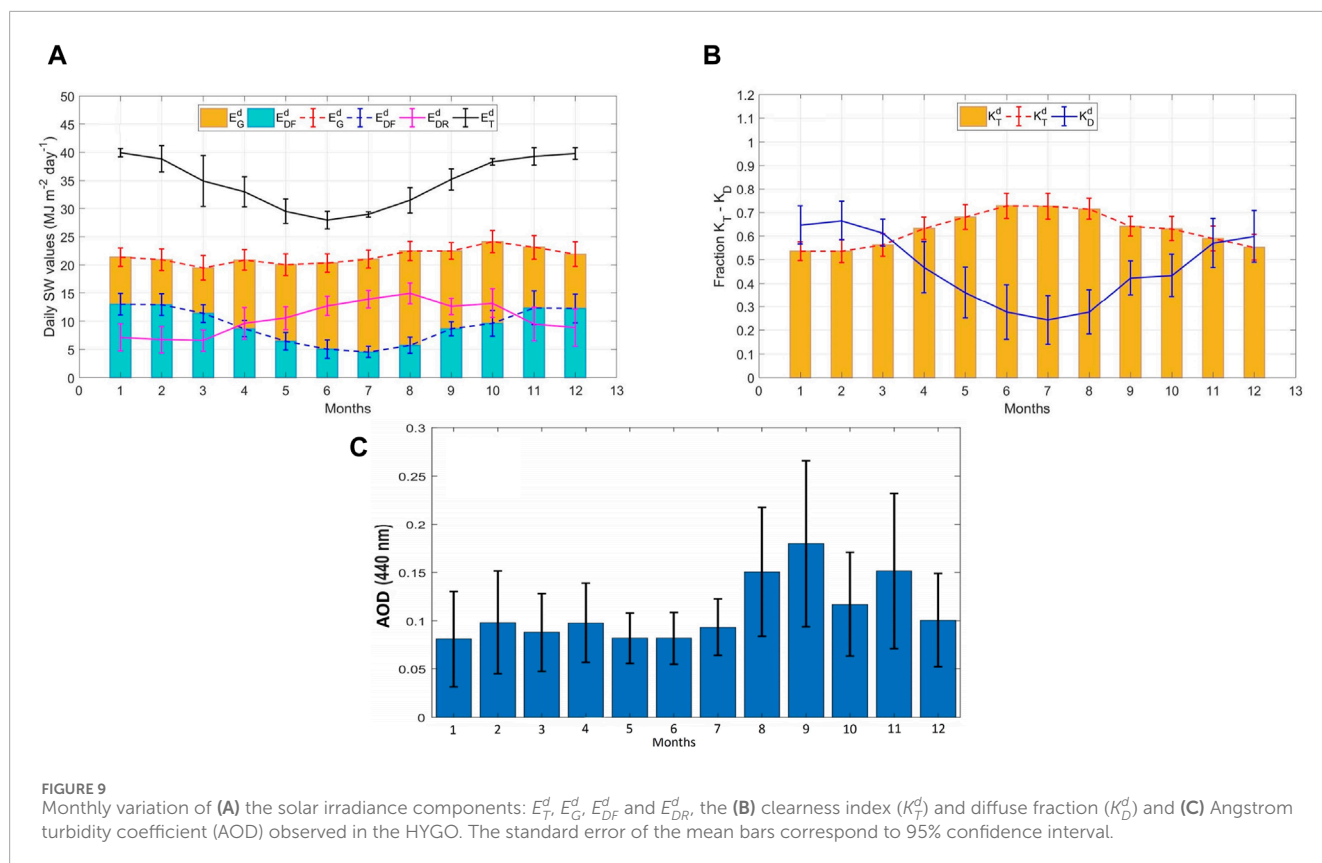
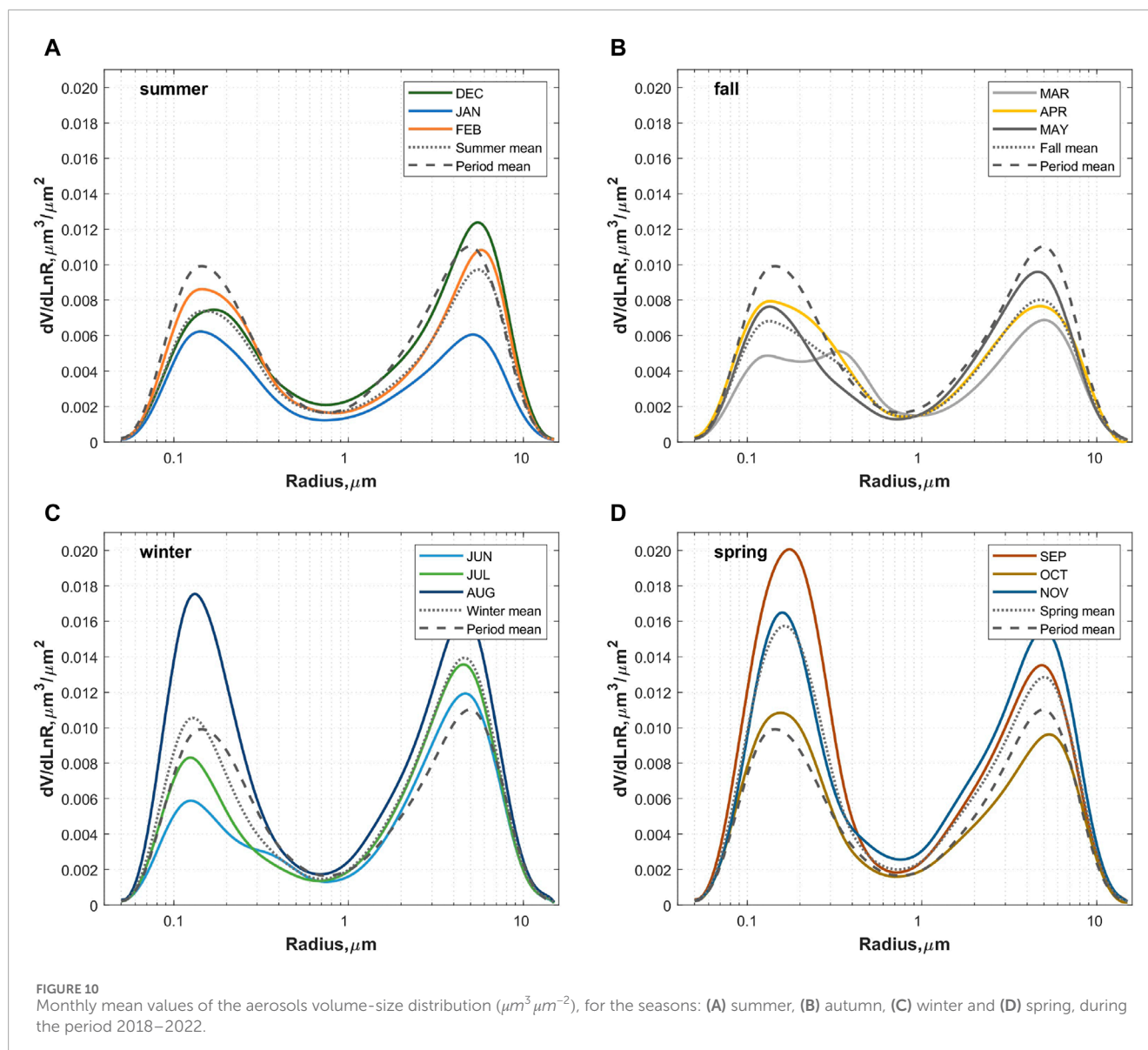


TABLE 2 Seasonally average daily values of solar irradiance components: E_T^d , E_G^d , E_{DF}^d and E_{DR}^d , clearness index (K_T) and diffuse fraction (K_D) observed in the HYGO. Also are shown the standard deviations for each component.

	Irradiances (MJ m ⁻² day ⁻¹)				Indexes	
	E_T	E_G	E_{DF}	E_{DR}	K_T	K_D
January	39.94±0.74	21.39±1.60	13.03±1.91	7.15±2.40	0.54±0.04	0.65±0.08
February	38.84±2.30	20.95±1.94	12.97±1.94	6.73±2.30	0.54±0.05	0.66±0.08
March	34.91±4.52	19.50±2.15	11.38±1.61	6.59±1.89	0.56±0.05	0.61±0.06
April	32.98±2.69	20.87±1.82	8.71±1.42	9.61±2.81	0.63±0.05	0.47±0.11
May	29.51±2.18	20.06±1.92	6.48±1.57	10.59±2.04	0.68±0.05	0.36±0.11
June	27.96±1.58	20.33±1.63	5.05±1.61	12.75±1.72	0.73±0.05	0.28±0.12
July	28.96±0.46	21.03±1.59	4.57±1.00	13.91±1.56	0.73±0.06	0.24±0.10
August	31.48±2.26	22.48±1.72	5.75±1.44	14.97±1.82	0.71±0.04	0.28±0.09
September	35.16±1.88	22.45±1.48	8.65±1.25	12.64±1.43	0.64±0.04	0.42±0.07
October	38.29±0.60	24.14±1.98	9.64±2.31	13.20±2.56	0.63±0.05	0.43±0.09
November	39.26±1.56	23.14±2.10	12.40±2.99	9.51±2.99	0.59±0.05	0.57±0.10
December	39.76±1.04	21.92±2.16	12.29±2.55	8.87±3.30	0.55±0.05	0.60±0.11



sunshine hours and increased E_T^d , leads to a rise in E_{DF}^d , ultimately resulting in higher E_G^d . This effect is particularly noticeable in October (Figure 9A), which still experiences many days with high sunshine hours (Figure 4D), reaching a maximum E_G^d intensity of $24.14 \text{ MJ m}^{-2} \text{ day}^{-1}$.

Moreover, during the study period, several high aerosol concentration events were recorded by the AERONET station's sun photometer, primarily in September. Notably, on 24 November 2020, at 21:23 UTC, the sun photometer recorded the highest AOD values since its installation on 19 March 2015, at HYGO, with an AOD 440 nm value of 1.23. These elevated AOD levels are linked to biomass-type aerosols. To determine if these aerosols were related to biomass burning, the HYSPLIT trajectory model was employed. Using NCEP reanalysis meteorological data, 120-h back-trajectories were calculated at three altitude levels: 500, 1,500, and 3000 m, from the sun photometer's location. Figure 11 presents these back-trajectories along with fire hotspots detected by the MODIS and VIIRS satellites, indicated as red dots. By

applying a coincidence criterion of a 4 km radius and 1 km height around the trajectory, two coincident fire hotspots were identified. These hotspots were located 281.2 km and 282.6 km from the sun photometer, at altitudes of 355.4 m and 343.1 m, respectively, where the 500 m back-trajectory passed. This evidence strongly suggests that the biomass-type aerosols observed on the specified date likely originated from these fire hotspots.

5.3 Irradiance empirical models

Initial modeling efforts in numerous countries focused on establishing a relationship between daily horizontal global irradiation and the duration of bright sunshine. The initial phase of this endeavor entailed the formulation of regression equations based on monthly-averaged data. However, subsequent advancements have led to the development of equations utilizing data recorded at daily intervals. This progression allows for a more comprehensive understanding by connecting the discussed relationships with the

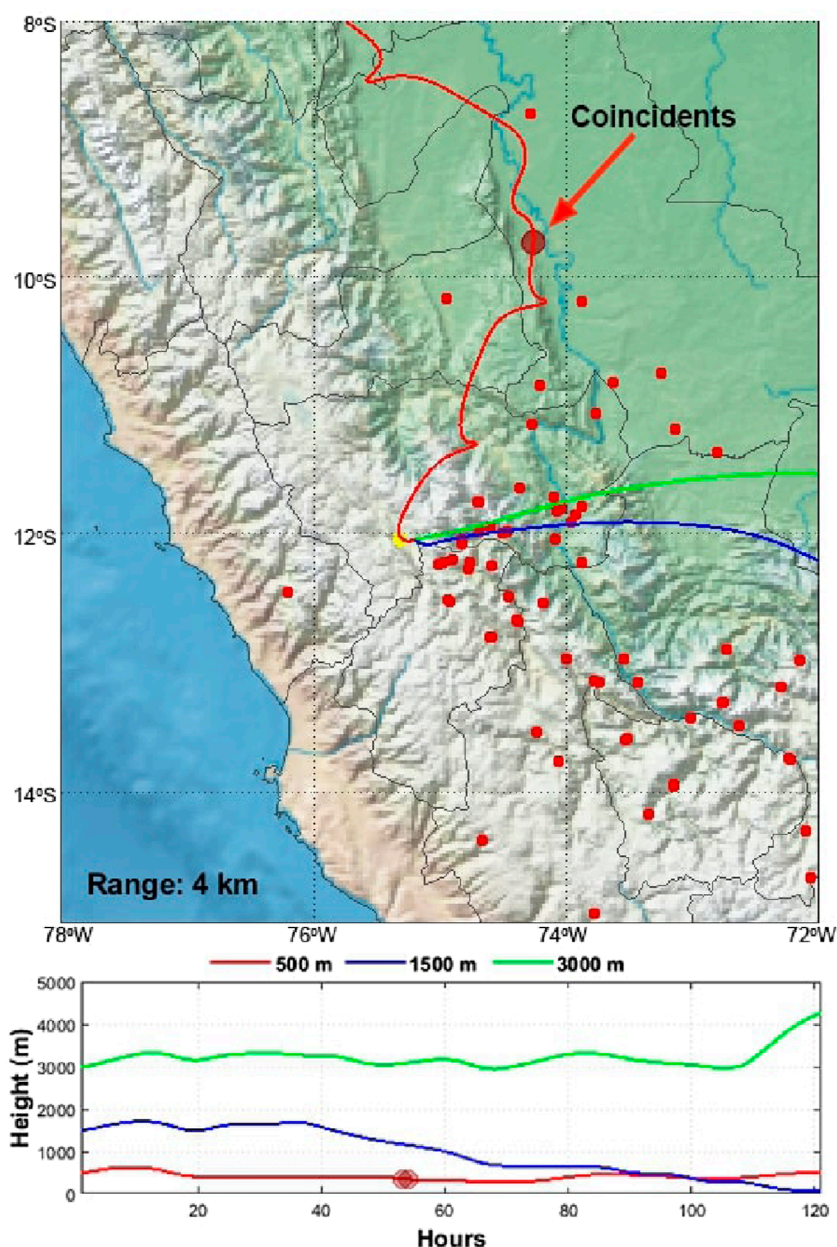


FIGURE 11

At the top, the red dots represent the fire hotspots associated with biomass burning. The yellow dot represents the position of the sun photometer at the HYGO, and the lines represent the back trajectories at 500 m (red line), 1,500 m (blue line), and 3000 m (green line) above the sun photometer at zero time. At the bottom, the back trajectories at different altitudes over the 120-h model run are shown.

daily variation between horizontal diffuse and global irradiation. This section will present an analysis enabling the estimation of diurnal horizontal global and diffuse irradiation at different time scales.

5.3.1 Monthly-averaged daily horizontal global (MADHG) and diffuse (MADHD) irradiation models

In this section, we introduce the MADHG irradiation model, designed to establish a connection between the monthly-averaged

daily clearness index ($K_T = E_G/E_T$) and the monthly mean daily sunshine fraction, as defined by Equations 2, 3. Figure 12A showcases a scatter plot for Equation 2, utilizing irradiance data from the BSRN station on the HYGO spanning from May 2017 to December 2022. Notably, a robust correlation between the variables is apparent, characterized by an R^2 value of 0.76 and a root mean squared error (RMSE) of approximately 4.1%. The coefficients 'a' and 'b' in Equation 2 are illustrated in Figure 12A; Table 3 as 0.33 and 0.50, respectively. It is noteworthy that analogous plots, depicting strong correlations with comparable 'a' and 'b' values, have been presented by various researchers for diverse sites worldwide (Munier, 2004b).

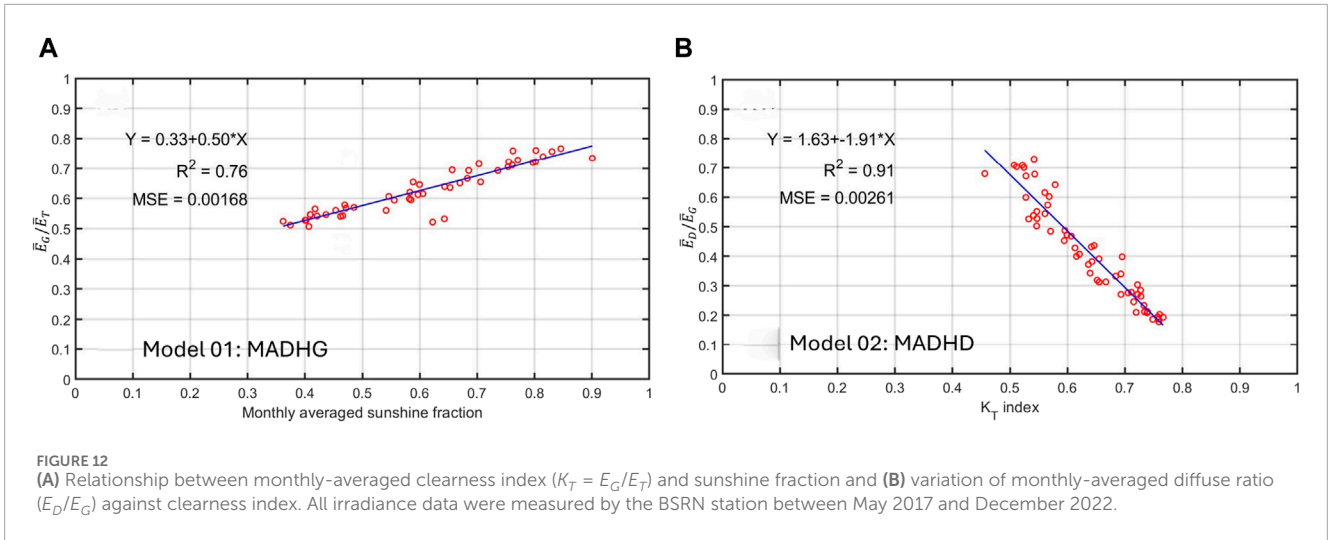


TABLE 3 Coefficients and statistical parameters for the empirical irradiance models. The forty percent (40%) of the total filtered dataset chosen randomly (740 days or 17 760 h) were reserved for rigorous statistical tests to evaluate model performance and robustness. The RMSE was calculated in percentage and in MJ m⁻² day⁻¹.

Irradiance Models	Coefficients				Statistics		
	a	b	c	d	r ²	RMSE (%)	RMSE (MJ)
Model 01: MADHG	0.33	0.50	-	-	0.76	4.1	0.88
Model 02: MADHD	1.63	-1.91	-	-	0.91	5.0	1.08
Model 03: DAHG	0.32	0.51	-	-	0.85	5.0	1.08
Model 04: DAHD	0.75	2.45	7.15	3.92	0.86	9.3	2.0

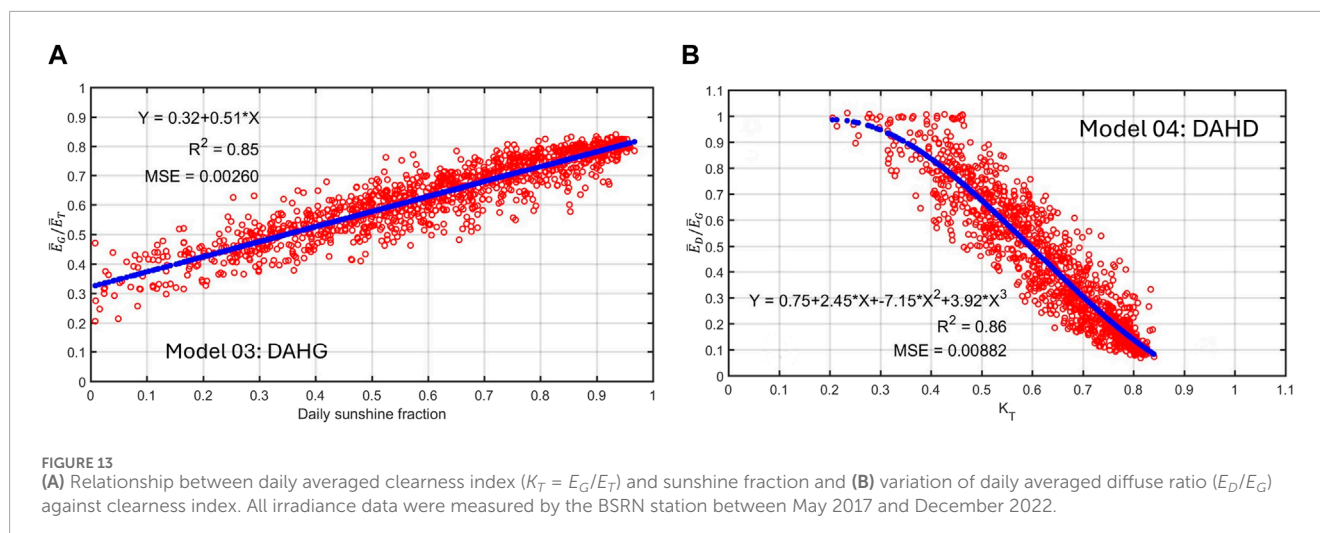
Furthermore, we introduced the MADHD irradiation model, designed to establish a relationship between the monthly-averaged daily diffuse ratio (E_D/E_G) and the monthly-averaged daily clearness index (K_T), as defined by Equation 4. Figure 12B illustrates the scatter plot for Equation 4, utilizing irradiance data from the BSRN station on the HYGO spanning from May 2017 to December 2022. Similar to the previous model, a robust correlation is evident between the discussed variables, characterized by an R^2 value of 0.91 and a root mean squared error (RMSE) of approximately 5%. The coefficients 'a' and 'b' in Equation 4 are depicted in Figure 12B; Table 3 as 1.63 and -1.91, respectively. It is noteworthy that analogous plots, demonstrating strong correlations with comparable 'a' and 'b' values, have been presented by various researchers for numerous sites worldwide (Munner, 2004c).

5.3.2 Daily-averaged horizontal global (DAHG) and diffuse (DAHD) irradiation models

In this section we present the irradiation model DAHG, which connect the daily clearness index ($K_T = E_G/E_T$) with

the daily sunshine fraction, according to the Equations 3, 5. Moreover, Figure 12B, shows the scatter plot for the Eq. Equation 5 using the irradiance data of the BSRN station on the HYGO between May 2017 and December 2022. A strong correlation between the two quantities under discussion is evident with R^2 equal to 0.85 and RMSE around 5%. Figure 13A also shows the coefficients 'a' and 'b' of the Eq. Equation 5; Table 3, equals to 0.32 and 0.51, respectively. In general, the relationships for daily values and monthly-averaged daily values, represented by Eqs Equations 2, 5, respectively, are different, according to Munner (2004d).

In addition, we introduced the DAHD irradiation model, designed to establish a connection between the daily diffuse ratio (E_D/E_G) and the daily clearness index ($K_T = E_G/E_T$), as expressed by Equation 4. Figure 13B displays the scatter plot for Equation 6, utilizing irradiance data from the BSRN station on the HYGO between May 2017 and December 2022. Mirroring the pattern observed in the previous model, a robust correlation is apparent between the two discussed variables, with an R^2 value of 0.86 and a mean squared error (MSE) of approximately 9.3%. Figure 12B and Table 3 also presents the coefficients 'a', 'b', 'c', and 'd' of Equation 6 as 0.75, 2.45, 7.15, and 3.92, respectively. Notably, analogous plots, demonstrating strong correlations with comparable values for 'a', 'b', 'c', and 'd', have been presented by various researchers



for numerous sites worldwide (Muneer and Hawas, 1984; Saluja et al., 1988).

5.3.3 Hourly horizontal global (HHG) and diffuse (HHD) irradiation models

In this section, we introduce the HHG irradiation model, which connect the ratio between the hourly global irradiation and the daily global irradiation (r_G) with the sunset hour angle expressed as radians from solar noon, according to the Equations 7, 8. Figure 14 illustrates the effect of the displacement of the hour from solar noon, and the daylength, on the ratio of hourly to daily global irradiation (r_G). There are six time deviations occurring before solar noon (-0.5 h, -1.5 h, -2.5 h, -3.5 h, -4.5 h, -5.5 h), depicted in Figure 14A, and six deviations occurring after solar noon ($+0.5$ h, $+1.5$ h, $+2.5$ h, $+3.5$ h, $+4.5$ h, $+5.5$ h), displayed in Figure 14B. The values of r_G range from around 0.15 at ± 0.5 h to 0.01 at ± 5.5 h and the values of sunset hour angle range from 1.48 (84.8°) at ± 0.5 h to 1.65 (94.5°) at ± 5.5 h. This narrow range of these values is due to the latitude location of the HYGO (12°).

Unlike certain previous studies (Liu and Jordan, 1960; Iqbal, 1983), which utilized a least-squares fit to determine the coefficients of Equations 7, 8, we employed a least-squares fit approach to ascertain these coefficients individually for each hour preceding and following solar noon. First column of Table 4 shows fitted values for the coefficients of r_G and statistical indicators for the hourly horizontal global (HHG) irradiation model fitting for each hour preceding and following solar noon. However, the values of R^2 range from 0.12 for $+4.5$ h to 0.83 for $+2.5$, and the values of RMSE range from 5.4% to 8.4%. It is important to note that these coefficient values within -4.5 and $+1.5$ h, are similar to those found by Iqbal (1983) testing the applicability of the model of Liu and Jordan (1960).

On the other hand, we also introduce the HHD irradiation model, which connect the ratio between the hourly diffuse irradiation and the daily diffuse irradiation (r_D) with the sunset hour angle expressed as radians from solar noon, according to the Equations 8, 10. Figure 15 illustrates the effect of the displacement of the hour from solar noon, and the daylength, on the ratio of hourly

to daily diffuse irradiation (r_D). As in the case of the global diffuse irradiation, there are six time deviations occurring before solar noon (-0.5 , -1.5 h, -2.5 h, -3.5 h, -4.5 h, -5.5 h), depicted in Figure 15A, and six deviations occurring after solar noon ($+0.5$, $+1.5$ h, $+2.5$ h, $+3.5$ h, $+4.5$ h, $+5.5$ h), displayed in Figure 15B. The values of r_D range from around 0.12 at ± 0.5 h to 0.015 at ± 1.5 h and the values of sunset hour angle range from 1.48 (84.8°) at ± 0.5 h to 1.66 (95.1°) at ± 5.5 h. This narrow range of these values is due to the latitude location of the HYGO (12°).

Second column of Table 4 shows fitted values for the coefficients of r_D and statistical indicators for the hourly horizontal diffuse (HHD) irradiation model fitting for each hour preceding and following solar noon. However, the values of R^2 range from 0.11 for -3.5 h to 0.89 for $+3.5$, and the values of RMSE range from 6.3% to 8.9%. It is important to note that there is a wide variety of values for the coefficients depending on the hours from solar noon, which indicates that the Equations 8, 10 may not be suitable for representing these variables.

5.3.4 Hourly diffuse correlation (HDC) irradiance models

In this study, the sigmoid logistic function is employed to depict the correlation between K_D^h and K_T^h . In comparison to alternative logistic functions Boland and Ridley (2008); Ridley et al. (2010), it demonstrates superior capability in capturing the behavior of K_D^h across all K_T^h values, particularly when K_T^h approaches unity. To construct the regression model, the total dataset spanning the years 2017–2022 is partitioned randomly into two segments, the first one for regression model development and the second one for conducting statistical tests.

For the performance evaluation of regression models, two key statistical parameters are employed: i) the coefficient of determination (R^2) and ii) root mean square error (RMSE). Figure 16 shows the scatter plot of K_D^h versus K_T^h (Liu-Jordan Diagram). The sigmoid function proposed in this work is compared with models developed for regions located in South Hemisphere (Oliveira et al., 2002a; Boland and Ridley, 2008; Marques Filho et al.,

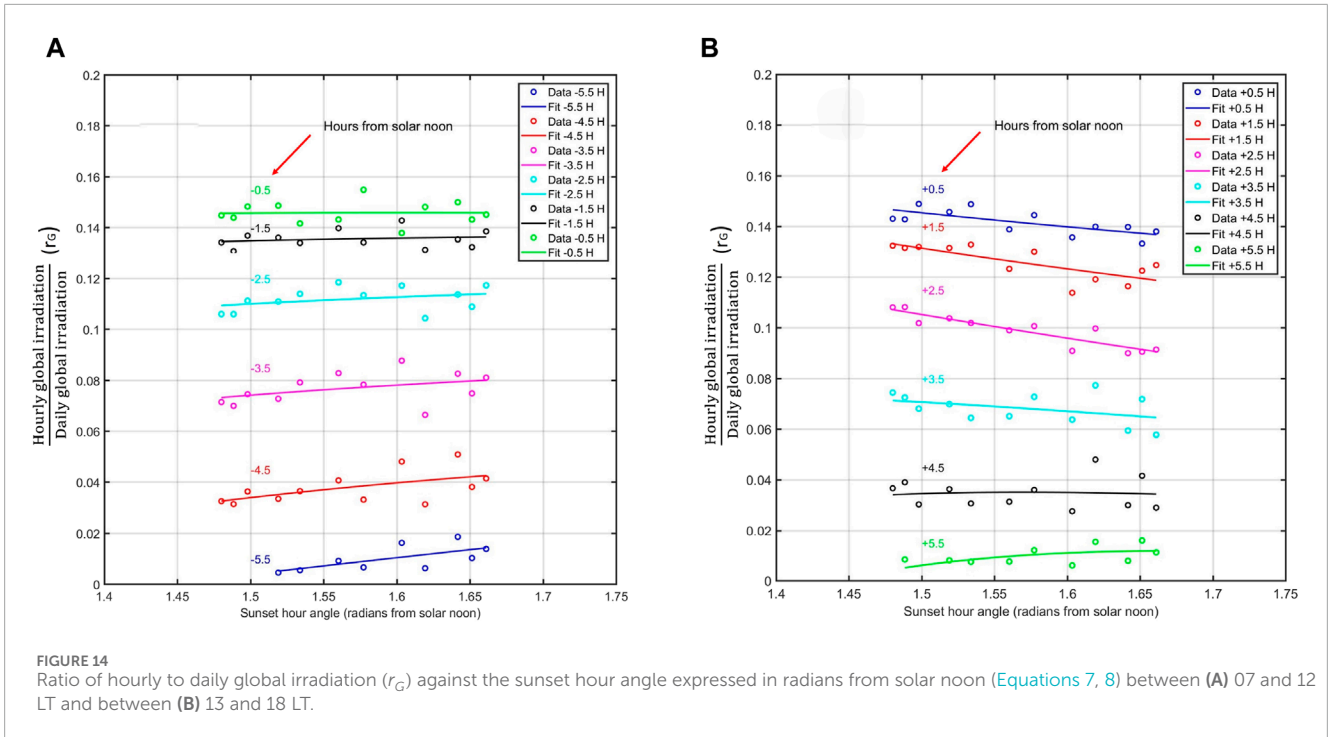
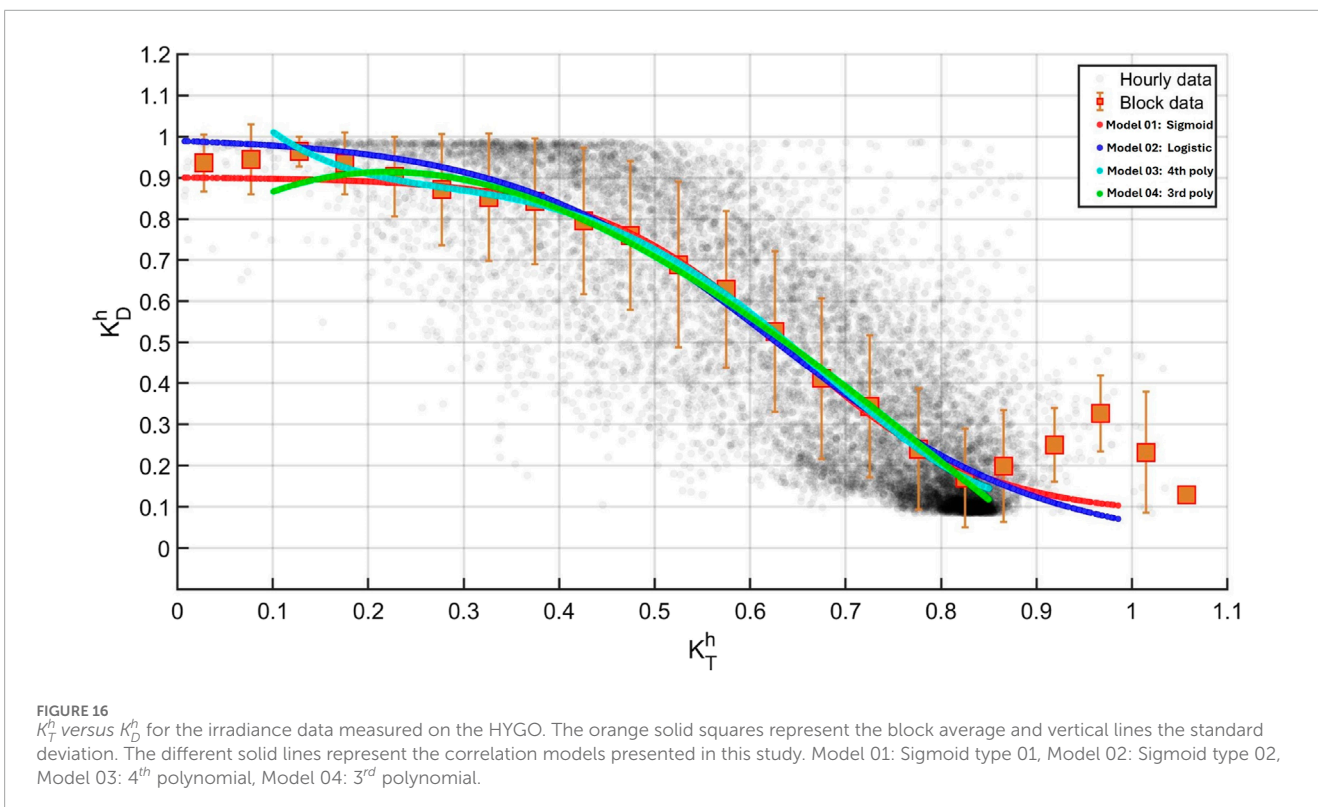
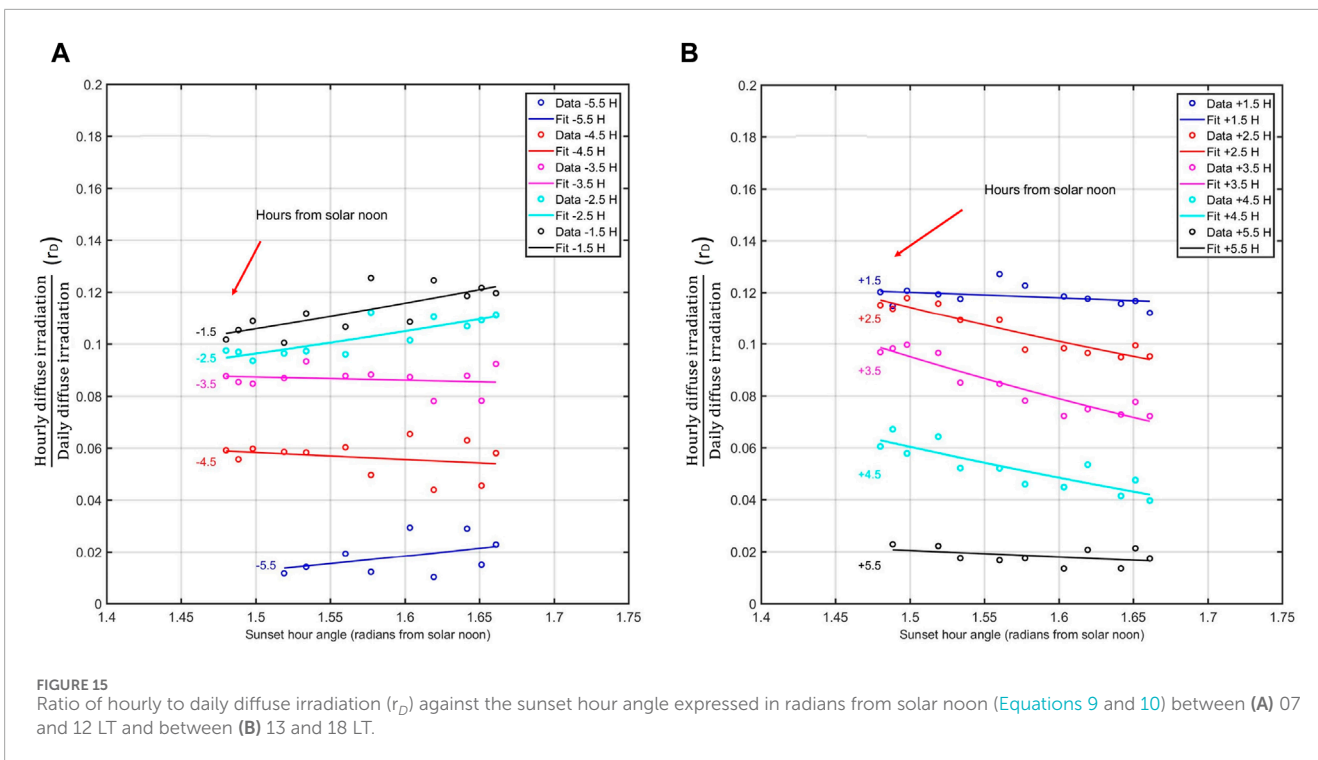


TABLE 4 Coefficients of r_G and r_D and statistical indicators for the hourly horizontal global (HHG) and diffuse (HHD) irradiation models fitting for each hour preceding and following solar noon. The forty percent (40%) of the total filtered dataset chosen randomly (740 days or 17 760 h) were reserved for rigorous statistical tests to evaluate model performance and robustness. The RMSE was calculated in percentage and in $\text{MJ m}^{-2} \text{hour}^{-1}$.

Hours from solar noon	r_G							r_D						
	Coefficients				Statistics			Coefficients				Statistics		
	r	s	p	q	R^2	RMSE (%)	RMSE (MJ)	t	u	v	w	R^2	RMSE (%)	RMSE (MJ)
-5.5	-0.02	0.94	0.53	-0.44	0.46	7.0	0.22	0.99	5.88	15.92	-2.01	0.19	8.9	0.28
-4.5	0.38	0.53	0.55	-0.49	0.32	7.7	0.24	9.02	-1.30	15.74	4.04	0.11	8.9	0.28
-3.5	0.41	0.69	0.54	-0.38	0.17	8.4	0.26	10.53	2.01	14.22	3.57	0.11	7.0	0.22
-2.5	0.36	0.84	0.49	-0.23	0.13	7.0	0.22	5.79	4.61	14.97	-2.89	0.69	7.0	0.22
-1.5	0.34	0.87	0.45	-0.16	0.12	6.3	0.20	5.44	5.35	14.86	-2.81	0.58	8.0	0.25
-0.5	0.33	0.87	0.43	-0.13	0.11	7.0	0.22	5.92	6.11	14.67	-1.62	0.43	8.9	0.28
+0.5	0.44	0.61	0.54	-0.39	0.53	6.3	0.20	7.49	6.06	14.27	0.19	0.40	7.0	0.22
+1.5	0.54	0.39	0.63	-0.60	0.59	7.0	0.22	11.86	4.27	12.42	5.02	0.15	6.3	0.20
+2.5	0.69	0.02	0.75	-0.88	0.83	5.4	0.17	0.09	-0.01	0.03	0.07	0.87	6.3	0.20
+3.5	0.72	-0.09	0.73	-0.86	0.16	8.3	0.26	0.02	0.02	-0.03	0.08	0.89	6.3	0.20
+4.5	0.85	-0.51	0.73	-0.89	0.12	8.3	0.26	1.12	-0.94	0.74	1.17	0.75	7.0	0.22
+5.5	1.28	-1.48	0.70	-0.76	0.15	6.3	0.20	0.10	-0.09	0.51	0.12	0.18	6.3	0.20



2016). It is important to highlight that this is the first study to utilize high-quality solar radiation data to develop empirical models of solar radiation in the central Andes of Peru.

The superiority of the sigmoid type 01 function becomes apparent when comparing its conformity to the

block-averaged experimental curve against other correlation models (Oliveira et al., 2002a; Jacovides et al., 2006; Boland and Ridley, 2008). Notably, while the logistic function adjusted to the HYGO dataset enhanced the statistical performance of that particular model, the sigmoid function consistently

TABLE 5 Equations fitted for K_D^h in function of K_T^h and statistical performance of the models for calculating the hourly averaged diffuse fraction K_D^h . The forty percent (40%) of the total filtered dataset chosen randomly (740 days or 17 760 h) were reserved for rigorous statistical tests to evaluate model performance and robustness. The RMSE was calculated in percentage and in MJ m⁻² hour⁻¹.

Models	Equation	r ²	RMSE (%)	RMSE (MJ)
Model 01: Sigmoid 0 ≤ K _T ≤ 1.0	$K_D = 0.1 + 0.83 \frac{1.0}{1 + \exp(-6.29 + 9.84 K_T)}$	0.831	14.9	0.47
Model 02: Logistic 0 ≤ K _T ≤ 1.0	$K_D = \frac{1.0}{1 + \exp(-4.52 + 7.20 K_T)}$	0.826	15.2	0.48
Model 03: 4 th polynomial K _T ≤ 0.15 0.1 < K _T ≤ 0.85 K _T ≥ 0.85	$K_D = 0.96$ $K_D = 1.3 - 3.9K_T + 14.7K_T^2 - 24.6K_T^3 + 12.7K_T^4$ $K_D = 0.15$	0.813	15.8	0.49
Model 04: 3 rd polynomial K _T ≤ 0.18 0.18 < K _T ≤ 0.85 K _T ≥ 0.85	$K_D = 0.94$ $K_D = 0.74 + 1.62K_T - 4.26K_T^2 + 1.74K_T^3$ $K_D = 0.12$	0.809	16.4	0.51

outperforms all alternatives, including 3rd and 4th polynomial functions.

The statistical parameters outlined in Table 5 indicate that all models present a coefficient of determination higher than 83%. Notably, the proposed sigmoid function fitting exhibits the best statistical performance, closely followed by the adjusted logistic and 4th polynomial functions, which show lower RMSE values. Nevertheless, all correlation models yield predictions that are statistically significant at a confidence level of 95%. These results closely resemble those reported by Marques Filho et al. (2016) for the city of Rio de Janeiro in Brazil. However, Marques Filho et al. (2016) did not make adjustments for polynomial functions, as they relied on the results of the study conducted by Oliveira et al. (2002a). This decision was due to the minimal divergence in climate conditions between Rio de Janeiro and São Paulo.

On the other hand, the AIC statistical method, assessed using Equations 11, 12, identifies the sigmoid function for HYGO as the best model (see Table 6). However, all correlation models are statistically relevant (Δ_iAIC < 2) (Burnham and Anderson, 2004) and can effectively reproduce the relationship between K_D^h and K_T^h . Although the logistic function proposed by Boland and Ridley (2008) relies on only two parameters, its performance when fitted to the HYGO dataset is not optimal. This is likely due to the curve of points (K_D^h , K_T^h) simulated by Boland and Ridley (2008) diverging significantly from the mean values (see Figure 16).

6 Discussions

6.1 Atmospheric variables

The first goal of the present study was to evaluate the climate characteristics of the western Mantaro Valley, using data from two meteorological stations: the HYGO conventional station and the IGP automatic station. It includes surface weather measurements from HYGO spanning 1981 to 2020 and 1-min averages from the IGP platform between 2017 and 2022. Details on the station

TABLE 6 Statistical performance of the sigmoid function model in comparison with the other empirical irradiance models for the HYGO.

Models	Number of parameters	AIC	Δ _i AIC
Model 01: Sigmoid	4	-3.655	0.000
Model 02: Logistic	2	-3.642	-0.013
Model 03: 4 th polynomial	7	-3.647	-0.008
Model 04: 3 rd polynomial	6	-3.639	-0.016

instrumentation are provided in recent publications (Flores-Rojas et al., 2019a; 2021; 2020).

Based on Köppen-Geiger classification (Peel et al., 2007) and data from the HYGO station, the Mantaro Valley is classified as Cwb, indicating a temperate climate with dry winters and warm summers. The criteria include a mean temperature of the hottest month above 10°C and the mean temperature of the coldest month between 0°C and 18°C. Precipitation patterns show the driest and wettest months receiving approximately 90 mm and 130 mm of rainfall respectively. Summer accumulation is 340 mm with a peak in February, while winter accumulation is 28 mm with a minimum in July. Maximum daily precipitation occurs in May and December, while the minimum is observed in June (Figure 3).

An alternative method for evaluating data from the HYGO automatic station involves using psychrometric diagrams to characterize seasonal climate conditions. There are moderate correlations between specific humidity (q) and temperature (T), with approximately 60% for mean diurnal averages and 75% for mean monthly averages. Daily q values range from 1.5 g kg⁻¹ in spring to 11 g kg⁻¹ in fall and summer, with RH fluctuating between 20% and 90%. Monthly average q varies from 4 g kg⁻¹ in winter to 10 g kg⁻¹ in fall and summer, with RH consistently between 40% and 75%. These analyses suggest that radiation measurements from the HYGO automatic station between 2017 and 2022 may reflect cooler and drier conditions compared to the climatological norm,

though mean surface solar irradiance (E_G) remains representative of the MV region's climate. However, components like E_{DF} and E_{DR} appear more sensitive to local climate and land-use factors.

6.2 Irradiance variables

The seasonal variation in E_G^h , especially at noon, exhibits a low amplitude, ranging from $3.02 \pm 0.18 \text{ MJ m}^{-2} \text{ h}^{-1}$ in fall to $3.32 \pm 0.22 \text{ MJ m}^{-2} \text{ h}^{-1}$ in spring, resulting in a seasonal amplitude close to $0.30 \text{ MJ m}^{-2} \text{ h}^{-1}$. This amplitude is notably lower than the amplitude variation for E_T^h , which is close to $0.90 \text{ MJ m}^{-2} \text{ h}^{-1}$. This pattern can be attributed to the opposing seasonal variations of the solar irradiance components E_{DF}^h and E_{DR}^h , which attenuate the seasonal variation of E_G^h . Specifically, E_{DF}^h peaks during summer and reaches its minimum in winter, while E_{DR}^h peaks in winter and reaches its minimum in summer.

During the spring, moderate values of E_{DF}^h and E_{DR}^h lead to the highest values of E_G^h during this season. This behavior is associated with reduced precipitation, moderate cloud cover, and the presence of aerosols, possibly from biomass burning in the HYGO during spring months, which was analyzed by [Estevan et al. \(2019\)](#). Moreover, diurnal patterns of K_T^h show maximum values at noon in winter and minimums in summer, whereas K_D^h displays an inverse behavior showing maximums at noon in summer and minimums in winter. The amplitude of seasonally average values between K_T^h and K_D^h is minimal in summer and maximal in winter, with intermediate values in fall and spring.

In addition, the monthly average daily solar radiation components at the HYGO corroborate the seasonal patterns observed in hourly irradiance variables. Peak values of E_G^d are evident in October (spring), contrasting with lowest values observed in March (autumn). Similarly, peak values of E_{DR}^d manifest in August (winter) and begins to decrease continuously in the following months attributable to heightened aerosol optical depth (AOD) and to the increase of cloudiness during this period ([Estevan et al., 2019](#)). In contrast, E_{DF}^d peaks in January (summer) and reaches its minimums in July (winter), mirroring the pronounced seasonal fluctuations of aerosols, clouds and precipitation in the HYGO ([Giráldez et al., 2020](#)).

Besides, the increase in AOD during September significantly raises K_D^d from 0.25 in August to 0.42 in September and October. Consequently, there is a reduction in E_{DR}^d and an increase in E_{DF}^d , similar to the findings of [Huaping et al. \(2021\)](#) in Wuhan, China. However, in October, E_{DF}^d slightly increases while E_{DR}^d remains almost constant compared to September, which results in a slight increase in E_G^d during October, reaching its highest value of the year. This behavior is attributed to specific biomass burning events near HYGO, which cause a sudden increase in AOD and alter the solar irradiance components E_{DF}^d and E_{DR}^d ([Estevan et al., 2019](#)).

Moreover, the monthly mean aerosol size distributions, measured by a CIMEL CE-318T sun photometer (AERONET network) ([Holben et al., 1998; 2001](#)) reveal a bimodal distribution, with coarse-mode aerosols ($5.0613 \mu\text{m}$) predominating in summer, fall, and winter, accounting for 56.3% of the cases. These aerosols are mainly from marine and desert sources. Fine-mode aerosols ($0.1482 \mu\text{m}$), which make up 43.7%, are primarily produced by fossil fuel combustion and biomass burning ([Estevan et al.,](#)

[2019](#)). During spring, fine-mode aerosols predominate, particularly in September and November. This is primarily due to biomass burning in the Peruvian Amazon, leading to high Aerosol Optical Depth (AOD) values measured at HYGO. Increased forward scattering in an aerosol-rich atmosphere results in more ground-reaching energy ([Iqbal, 1983](#)). In spring, the presence of a large quantity of aerosols, coupled with longer sunshine hours, cloudiness and higher E_T^d , raises E_{DF}^d , leading to increased E_G^d . This behavior is especially evident in October, which experiences high sunshine hours and reaches a maximum values of E_G^d .

6.3 Irradiance models

The MADHG irradiation model establishes a connection between the monthly-averaged daily clearness index (K_T) and the monthly mean daily sunshine fraction. Utilizing irradiance data from the BSRN station on the HYGO, a strong correlation, with $R^2 = 0.76$, and RMSE of 4.1% are observed. Additionally, the DAHG irradiation model links the daily clearness index ($K_T = E_G/E_T$) to the daily sunshine fraction, revealing a strong correlation between the two variables, with R^2 equal to 0.85 and RMSE around 5.0%. It is noted that the relationships derived from the MADHG and DAHG models exhibit slight differences, as reported by [Munner \(2004d\)](#).

Furthermore, the MADHD irradiation model is designed to establish a relationship between the monthly-averaged daily diffuse ratio (E_D/E_G) and the monthly-averaged daily clearness index (K_T). In this case, a more robust correlation is evident between the discussed variables, characterized by an R^2 value of 0.91 and RMSE of approximately 5.0%. In addition, the DAHD irradiation model, designed to establish a connection between the daily diffuse ratio (E_D/E_G) and the daily clearness index (K_T), mirroring the pattern observed in the previous model, a robust correlation is apparent between the two discussed variables, with an R^2 value of 0.86 and RMSE of approximately 9.3%.

On the other hand, the HHG irradiation model links the ratio of hourly global irradiation to daily global irradiation (r_G) with the sunset hour angle expressed in radians from solar noon. Statistical indicators for this model reveal R^2 values ranging from 0.12 for +4.5 h from solar noon to 0.83 for +2.5 h from solar noon, with RMSE values spanning from 5.4% to 8.4%. Interestingly, coefficient values within the -4.5 h and +1.5 h range closely resemble those from prior studies [Iqbal \(1983\); Liu and Jordan \(1960\)](#).

Similarly, the HHD irradiation model links the ratio of hourly diffuse irradiation to daily diffuse irradiation (r_D) with the sunset hour angle in radians from solar noon. Its statistical indicators demonstrate R^2 values ranging from 0.11 for -3.5 h from solar noon to 0.89 for +3.5 h from solar noon, and RMSE values ranging from 6.3% to 8.9%. Notably, a wide range of coefficient values across hours from solar noon suggests that the mathematical expressions for this model may not comprehensively represent these variables.

The correlation models for hourly diffuse irradiance utilizes several function to correlate K_D^h and K_T^h . The present contribution shows that the sigmoid logistic function demonstrates superior performance, particularly when K_T^h approaches unity, compared to alternative functions. Evaluation metrics include R^2 and RMSE. The sigmoid function is compared favorably to models developed for the Southern Hemisphere, showing its first application in developing

empirical solar radiation models for Peru's central Andes. Superior performance of the sigmoid function is evident when compared to other models, including the logistic function adjusted to HYGO dataset and polynomial functions. All models exhibit R^2 values over 83%, with the sigmoid function showing the best statistical performance. The AIC method identifies the sigmoid function as the best model for HYGO, though all models effectively capture the K_D^h and K_T^h relationship.

It is important to highlight that the clearness index (K_T^h) is not independent of the zenith angle (θ_Z). A given K_T^h value represents significantly different conditions depending on whether the sun is near the zenith or the horizon. This approach inherently carries an error. Better performance can be achieved by using another variable, independent of θ_Z , to characterize insolation conditions. Another well-known limitation of K_T^h is that, for a given K_T^h value within a specific range of solar elevation, the atmospheric conditions can vary significantly in terms of direct and diffuse content. Additionally, other independent atmospheric variables can be incorporated if they provide relevant information about direct irradiance transmission. (Perez et al., 1990). For instance, surface dew-point temperature (T_d) serves as a reliable estimator of atmospheric precipitable water, which significantly influences both absorption and aerosol growth. This, in turn, affects the balance between direct and diffuse irradiance, as well as the scattering and direct-to-diffuse ratio (Perez et al., 1992).

For the present study, we propose models that use the hourly clearness index (K_T^h) to estimate (K_D^h) (Erbs et al., 1982), due to their simplicity and their status as the first proposed models. However, several other models, which perform marginally better than the currently used models for various global locations, will be implemented in future research. These models incorporate additional atmospheric variables such as the hourly clearness index and solar elevation (Maxwell, 1987; Skartveit and Olseth, 1987), hour-to-hour variability index and regional surface albedo (Skartveit and Olseth, 1987), dew-point temperature and hour-to-hour variability index (Perez et al., 1992), and apparent solar time with a measure of global radiation persistence (Ridley et al., 2010). These enhanced models will be incorporated in future studies to improve performance.

7 Conclusion

The present study evaluates the climatic characteristics of the western Mantaro Valley using data from the HYGO conventional station (1981–2020) and the IGP automatic station (2017–2022). The Mantaro Valley is classified as Cwb according to the Köppen-Geiger system, indicating a temperate climate with dry winters and warm summers. Summer sees peak precipitation, reaching 340 mm month⁻¹ in February, while winter experiences minimal precipitation, with 28 mm month⁻¹ in July. The analysis suggests that radiation measurements accurately represent the valley's climate, while factors like E_{DF} and E_{DR} are more influenced by local climate and land-use, indicating cooler and drier conditions compared to the regional climatic norms.

The analysis of diurnal and seasonal variations in E_{DR} , E_{DF} , and E_G in the western Mantaro Valley shows distinct patterns. At noontime, E_{DR}^h peaks during winter and decreases in summer.

Conversely, E_{DF}^h reaches its maximum in summer and declines in winter. Additionally, E_G^h peaks in spring and decreases in winter, influenced by astronomical factors, cloudiness, and aerosol concentrations observed from 2017 to 2022. Seasonal variations in daily solar radiation components at the HYGO surface reveal that E_{DR}^d peaks in winter, notably in August, with the lowest values in March. Conversely, peak E_{DF}^d values occur in summer, particularly in January, with the lowest values observed in winter, especially in July.

Notably, peak values of E_G^d occurred during spring, reaching its highest recorded value in October (24.14 MJ m⁻² day⁻¹) and its lowest in March (19.50 MJ m⁻² day⁻¹). This seasonal variation in E_G^d correlates with periods of biomass burning, which are associated with elevated aerosol optical depth (AOD) levels in the Mantaro Valley region. Biomass burning events typically occur from July to October annually, with September exhibiting peak AOD values. These months coincide with increased forest fire activity, both locally in Peru and in neighboring countries like Brazil and Bolivia. The influx of biomass-burning aerosols contributes to higher AOD levels in September, affecting K_D^d and consequently reducing E_{DR}^d while increasing E_{DF}^d . In October, E_{DF}^d shows a slight increase while E_{DR}^d remains constant, resulting in the peak of E_G^d for the year. This behavior is attributed to biomass burning events near the HYGO station.

This study investigates irradiation models that establish robust correlations among various solar radiation parameters. The MADHG and DAHG models relate the monthly-averaged daily clearness index (K_T) to daily sunshine fraction, while the MADHD and DAHD models connect the monthly-averaged daily diffuse ratio (E_D/E_G) to K_T . Furthermore, the HHG and HHD models correlate the ratio of hourly global or diffuse irradiation to daily values with the sunset hour angle. All these models demonstrated acceptable accuracy in predicting irradiance variables. Moreover, the sigmoid logistic function emerges as the most effective in correlating K_D^h and K_T^h , demonstrating superior performance compared to alternative functions and exhibiting strong statistical significance. The AIC method supports the superiority of the sigmoid function, emphasizing its efficacy in capturing the relationship between solar radiation components. It effectively reproduces the behavior of K_D^h as a function of K_T^h , demonstrating superior statistical performance compared to other correlation models.

It is important to emphasize that this is the first study aimed at the observational characterization and empirical modeling of global and diffuse solar irradiances in the central Peruvian Andes, using high-quality radiation data from sensors belonging to the BSRN network. In the future, this new model will be tested with E_{DF} and E_G measurements collected in other regions of central Andes and will be proposed better empirical models, physical parametric broadband models, perceptron neural-network techniques to estimate hourly values of the diffuse solar irradiance and machine learning methods for solar radiation forecasting. However, the empirical models presented here can easily be used to forecast solar irradiance components with acceptable accuracy, just like the proposals made for other South American cities. Future research should incorporate models that use additional atmospheric and solar variables for improved performance, such as solar elevation, hour-to-hour variability index, regional surface albedo, dew-point temperature and apparent solar time with a measure of global radiation persistence.

Data availability statement

The raw data supporting the conclusions of this article will be made available by the authors, without undue reservation.

Author contributions

OF-R: Writing–original draft, Methodology, Investigation, Formal Analysis, Conceptualization. JF-R: Writing–review and editing, Writing–original draft, Validation, Supervision, Methodology, Investigation, Formal Analysis, Data curation, Conceptualization. RE-A: Writing–review and editing, Validation, Supervision, Software, Formal Analysis, Data curation, Conceptualization. LG-S: Writing–review and editing, Investigation, Formal Analysis, Data curation. LS-S: Writing–review and editing, Validation, Supervision, Software, Resources, Formal Analysis. ES-P: Writing–review and editing, Software, Resources, Project administration. HK: Writing–review and editing, Visualization, Validation, Supervision, Software. YS: Writing–review and editing, Supervision, Resources, Project administration, Funding acquisition.

Funding

The author(s) declare that financial support was received for the research, authorship, and/or publication of this article. This work was done using computational resources, HPC-Linux-Cluster, from “Laboratorio de Dinámica de Fluidos Geofísicos Computacionales at Instituto Geofísico del Perú” (grants 101-2014-FONDECYT, SPIRALES2012 IRD-IGP, Manglares IGP-IDRC, PP068 program). The first author was supported by the Universidad Nacional Mayor de San Marcos – RR N° 006081-2023-R/UNMSM and project number B23131461. We also wish to thank to the “PROCIENCIA”

References

- Albarracín, G. (2017). Urban form and ecological footprint: urban form and ecological footprint: a morphological analysis for harnessing solar energy in the suburbs of Cuenca, Ecuador. *Energy Procedia* 115, 332–343. doi:10.1016/j.egypro.2017.05.030
- Álvarez, J., Mitsova, H., and Allen, H. (2011). Estimating monthly solar radiation in south-central Chile. *Chil. J. Agric. Res.* 71, 601–609. doi:10.4067/s0718-58392011000400016
- Angstrom, A. (1924). On the computation of global radiation from records of sunshine. *Ark. Geof. 2* (22), 471.
- Arya, S. (2005). Micrometeorology and atmospheric boundary layer. *Pure Applied Geophys.* 162, 1721–1745. doi:10.1007/3-7643-7377-6_2
- Bacher, P., Madsen, H., Perers, B., and Nielsen, H. (2013). A non-parametric method for correction of global radiation observations. *Sol. Energy* 88, 13–22. doi:10.1016/j.solener.2012.10.024
- Barragán-Escandón, E., Zalamea-León, E., Calle-Sigüencia, T.-J. J., and Terrados-Cepeda, J. (2022). Impact of solar thermal energy on the energy matrix under equatorial andean context. *Energies* 15 (16), 5803. doi:10.3390/en15165803
- Blumthaler, M., Ambach, W., and Ellinger, R. (1997). Increase in solar uv radiation with altitude. *J. Photochem. Photobiol. B Biol.* 39, 130–134. doi:10.1016/s1011-1344(96)0018-8
- Boland, B., and Ridley, J. (2008). *Modelling solar radiation at the Earth's surface*. Springer-Verlag, 193–219.
- Boor, C. (2001). in *Practical guide to splines. Applied mathematical science*. Editors J. E. Marsden, and L. Sirovich (New York: Springer-Verlag), 27, 354.
- Burnham, K., and Anderson, D. (2004). Multimodel inference: understanding aic and bic in model selection. *Sociol. Methods and Res.* 33, 261–304. doi:10.1177/0049124104268644
- Ceballos, J., Porfírio, A., Oricchio, P., and Posse, G. (2022). Characterization of the annual regime of surface solar irradiance over Argentine Pampean region using gl1. 2 satellite-based data. *Renew. Energy* 194, 526–537. doi:10.1016/j.renene.2022.05.038
- Cede, A., Luccini, E., Nuñez, L., Piacentini, R., and Blumthaler, M. (2002). Monitoring of erythemal irradiance in the Argentine ultraviolet network. *J. Geophys. Res. Atmos.* 107 (AAC 1–1–AAC 1–10). doi:10.1029/2001jd001206
- Codato, G., Oliveira, A., Soares, J., Escobedo, J., Gomes, E., and Pai, A. (2008). Global and diffuse solar irradiances in urban and rural areas in southeast Brazil. *Theor. Appl. Climatol.* 93 (1–2), 57–73. doi:10.1007/s00704-007-0326-0
- Collares-Pereira, M., and Rabl, A. (1979). The average distribution of solar radiation—correlations between diffuse and hemispherical and between daily and hourly insolation values. *Sol. Energy* 22, 155–164. doi:10.1016/0038-092x(79)90100-2
- Cordero, R., Seckmeyer, G., Damiani, A., Riechelmann, S., Rayas, F., Labbe, J., et al. (2014). The world's highest levels of surface uv. *Photochem. Photobiol. Sci.* 13(1), 70–81. doi:10.1039/c3pp50221j
- Cowley, J. (1978). The distribution over Great Britain of global solar radiation on a horizontal surface. *Meteorol. Mag.* 107, 357.
- Della-Ceca, L., Micheletti, M. I., Freire, M., Garcia, B., Mancilla, S. G. M. A., Crinó, E., et al. (2019). Solar and climatic high performance factors for the placement of solar

(N° PE501080424-2022-PROCIENCIA) for the financial support during the research period, in the context to the project: Biomass Burning and Impacts in the Southern Tropics with financial scheme E070-2022-01.

Acknowledgments

This work was done using computational resources, HPC-Linux-Cluster, from “Laboratorio de Dinámica de Fluidos Geofísicos Computacionales at Instituto Geofísico del Perú” (grants 101-2014-FONDECYT, SPIRALES2012 IRD-IGP, Manglares IGP-IDRC, PP068 program). Also, we wish to thank to the Instituto Geofísico del Perú and to the Universidad Nacional Mayor de San Marcos for logistic support for the authors during the development of the present research. Finally, we want to thank to the ChatGPT 4.0 from OpenAI to improve the English style of the manuscript.

Conflict of interest

The authors declare that the research was conducted in the absence of any commercial or financial relationships that could be construed as a potential conflict of interest.

Publisher's note

All claims expressed in this article are solely those of the authors and do not necessarily represent those of their affiliated organizations, or those of the publisher, the editors and the reviewers. Any product that may be evaluated in this article, or claim that may be made by its manufacturer, is not guaranteed or endorsed by the publisher.

- power plants in Argentina andes sites—comparison with african and asian sites. *ASME J. Sol. Energy Eng.* 141 (4), 041004. doi:10.1115/1.4042203
- De Souza, J., Lyra, C. G. B., Santos, D., Junior, C., Tiba, R. A. F., Lyra, G., et al. (2016). Empirical models of daily and monthly global solar irradiation using sunshine duration for alagoas state, northeastern Brazil. *Sustain. Energy Technol. Assess.* 14, 35–45. doi:10.1016/j.seta.2016.01.002
- Driemel, A., Augustine, J., Behrens, K., Colle, S., Cox, C., Cuevas-Agulló, E., et al. (2018). Baseline surface radiation network (bsrn): structure and data description (1992–2017). *Earth Syst. Sci.* 10, 1491–1501. doi:10.5194/essd-10-1491-2018
- Ellabban, O., Abu?Rub, H., and Blaabjerg, F. (2014). Renewable energy resources: current status, future prospects and their enabling technology. *Renew. Sustain. Energy Rev.* 39, 748–764. doi:10.1016/j.rser.2014.07.113
- Erbs, D., Klein, S., and Duffie, J. (1982). Estimation of the diffuse radiation fraction for hourly, daily and monthly average global radiation. *Sol. Energy* 28, 293–302. doi:10.1016/0038-092x(82)90302-4
- Espinoza-Villar, J., Ronchail, J., Guyot, J., Cochonneau, G., Naziano, F., Lavado, W., et al. (2009). Spatio-temporal rainfall variability in the amazon basin countries (Brazil, Peru, Bolivia, Colombia, and Ecuador). *Int. J. Climatol.* 29, 1574–1594. doi:10.1002/joc.1791
- Estevan, R., Martínez-Castro, D., Suarez-Salas, L., Moya, A., and Silva, Y. (2019). First two and a half years of aerosol measurements with an aeronet sunphotometer at the huancayo observatory, Peru. *Atmos. Environ.* 3, 100037. doi:10.1016/j.aeoa.2019.100037
- Ferreira, M., Oliveira, A., Soares, J., Codato, G., Bárbaro, J., and Escobedo, E. (2012). Radiation balance at the surface in the city of são paulo, Brazil. diurnal and seasonal variations. *Theor. Appl. Climatol.* 107, 229–246. doi:10.1007/s00704-011-0480-2
- Flores-Rojas, J., Cuxart, J., Piñas-Laura, M., Callañaupa, L. S., Suárez-Salas, Kumar, S., et al. (2019a). Seasonal and diurnal cycles of surface boundary layer and energy balance in the central andes of peru, mantaro valley. *Atmosphere* 10, 779. doi:10.3390/atmos10120779
- Flores-Rojas, J., Moya-Alvarez, A., Kumar, S., Martínez-Castro, D., Villalobos-Puma, E., and Silva-Vidal, Y. (2019b). Analysis of possible triggering mechanisms of severe thunderstorms in the tropical central andes of Peru, mantaro valley. *Atmosphere* 10 (6), 301–331. doi:10.3390/atmos10060301
- Flores-Rojas, J., Moya-Alvarez, J., Valdivia-Prado, A. S., Piñas-Laura, M., Kumar, S., Karam, H., et al. (2020). On the dynamic mechanisms of intense rainfall events in the central andes of Peru, mantaro valley. *Atmos. Res.* 248, 105188. doi:10.1016/j.atmosres.2020.105188
- Flores-Rojas, J., Silva, Y., Suárez-Salas, L., Estevan, R., Valdivia-Prado, J., Saavedra, M., et al. (2021). Analysis of extreme meteorological events in the central andes of Peru using a set of specialized instruments. *Atmosphere* 12, 408. doi:10.3390/atmos12030408
- Frohlich, C., and Lean, J. (1998). The sun's total irradiance: cycles, trends and related climate change uncertainties since 1976. *Geophys. Res. Lett.* 25, 4377–4380. doi:10.1029/1998gl900157
- Gaffen, D., and Ross, R. (1999). Climatology and trends of u.s. surface humidity and temperature. *J. Clim.* 12, 811–828. doi:10.1175/1520-0442(1999)012<0811:catous>2.0.co;2
- Garg, H., and Garg, S. (1985). Correlation of monthly-average daily global, diffuse and beam radiation with bright sunshine hours. *En. Conv. Mgmt.* 25, 409–417. doi:10.1016/0196-8904(85)90004-4
- Giráldez, L., Silva, Y., Zubieta, R., and Sulca, J. (2020). Change of the rainfall seasonality over central Peruvian andes: onset, end, duration and its relationship with large-scale atmospheric circulation. *Climate* 8 (23), 23. doi:10.3390/cli8020023
- Gomes, L., Marques Filho, E., Pepe, I., Mascarenhas, B. S., De Oliveira, A., De, A., et al. (2022). Solar radiation components on a horizontal surface in a tropical coastal city of salvador. *Energies* 15 (3), 1058. doi:10.3390/en15031058
- Gueymard, C. (2005). Importance of atmospheric turbidity and associated uncertainties in solar radiation and luminous efficacy modelling. *Energy* 30, 1603–1621. doi:10.1016/j.energy.2004.04.040
- Hastenrath, S. (1997). Measurements of solar radiation and estimation of optical depth in the high andes of Peru. *Meteorol. Atmos. Phys.* 64, 51–59. doi:10.1007/bf01044129
- Hawas, M., and Muneer, T. (1984). Study of diffuse and global radiation characteristics in India. *En. Conv. Mgmt.* 24, 143–149. doi:10.1016/0196-8904(84)90026-8
- Holben, B., Eck, T., Slutsker, I., Tanre, D., Buis, J., Setzer, A., et al. (1998). Aeronet – a federated instrument network and data archive for aerosol characterization. *Rem. Sens. Environ.* 66, 1–16. doi:10.1016/s0034-4257(98)00031-5
- Holben, B., Tanré, D., Smirnov, A., Eck, T., Slutsker, I., Abuhassan, N., et al. (2001). An emerging ground-based aerosol climatology: aerosol optical depth from aeronet. *J. Geophys. Res.* 106 (D11), 12067–12097. doi:10.1029/2001jd900014
- Huaping, L., Ming, Z., Lunche, W., Yingying, M., Wenmin, Q., and Wei, G. (2021). The effect of aerosol on downward diffuse radiation during winter haze in wuhan, China. *Atmos. Environ.* 265, 118714. doi:10.1016/j.atmosenv.2021.118714
- Iqbal, M. (1983). *An introduction to solar irradiation*. Toronto: Academic Press, 390.
- Jacovides, C., Tymvios, F., Assimakopoulos, V., and Kaltsounides, N. (2006). Comparative study of various correlations in estimating hourly diffuse fraction of global solar radiation. *Renew. Energy* 31, 2492–2504. doi:10.1016/j.renene.2005.11.009
- Jager Waldau, A. (2019). *PV status report 2019*. Luxembourg: Publications Office of the European Union, 7–94.
- Janjai, S., Pankaew, P., and Laksanaboonson, J. (2009). A model for calculating hourly global solar radiation from satellite data in the tropics. *Appl. Energy* 86, 1450–1457. doi:10.1016/j.apenergy.2009.02.005
- Journee, M., and Cedric, B. (2010). Quality control of solar radiation data within the rmib solar measurements network. *Sol. Energy* 85, 72–86. doi:10.1016/j.solener.2010.10.021
- Le Baron, B., and Dirmhirn, I. (1983). Strengths and limitations of the liu and jordanmodel to determine diffuse from global irradiance. *Sol. Energy* 31, 167–172. doi:10.1016/0038-092x(83)90078-6
- Liu, B., and Jordan, R. (1960). The interrelationship and characteristic distribution of direct, diffuse and total solar radiation. *Sol. Energy* 4, 1–19. doi:10.1016/0038-092x(60)90062-1
- Luccini, E., Cede, A., Piacentini, R., Villanueva, C., and Canziani, P. (2006). Ultraviolet climatology over Argentina. *J. Geophys. Res. Atmos.* 111. doi:10.1029/2005jd006580
- Marques Filho, E., Oliveira, A., Vita, W., Mesquita, F., Codato, G., Escobedo, J., et al. (2016). Global, diffuse and direct solar radiation at the surface in the city of rio de janeiro: Observational characterization and empirical modeling. *Renew. Energy* 91, 64–74. doi:10.1016/j.renene.2016.01.040
- Martins, F., Pereira, E., and Abreu, S. (2007). Satellite-derived solar resource maps for Brazil under swera project. *Sol. Energy* 81, 517–528. doi:10.1016/j.solener.2006.07.009
- Maxwell, E. (1987). *A quasi-physical model for converting hourly global horizontal to direct normal insolation*. Golden, CO: Solar Energy Research Institute. Report SERI/TR-215-3087, –.
- McKenzie, P. R. L., Aucamp, Bais, A., Björn, L., Ilyas, U., and Madronich, S. (2011). Ozone depletion and climate change: impacts on uv radiation. *Photochem. Photobiological Sci.* 10(2), 182–198. doi:10.1039/c0pp90034f
- Monteith, J., and Unsworth, M. (1990). *Principles of environmental Physics*. London: Edward Arnold, 291 edn. first.
- Motulsky, H., and Arthur, C. (2003) “Fitting models to biological data using linear and nonlinear regression: a practical guide to curve fitting. New York, NY: online edn, Oxford Academic. doi:10.1093/oso/9780195171792.001.0001 (Accessed 01 August, 2024)
- Muneer, T., and Hawas, M. (1984). Correlation between daily diffuse and global radiation for India. *En. Conv. Mgmt.* 24, 151–154. doi:10.1016/0196-8904(84)90027-x
- Munner, T. (2004a). *Solar Radiation and daylight models*. Elsevier Butterworth Heinemann, 37.
- Munner, T. (2004b). *Solar Radiation and daylight models*. Elsevier Butterworth Heinemann, 39.
- Munner, T. (2004c). *Solar Radiation and daylight models*. Elsevier Butterworth Heinemann, 42.
- Munner, T. (2004d). *Solar Radiation and daylight models*. Elsevier Butterworth Heinemann, 52.
- Oliveira, A., Machado, A., Escobedo, J., and Soares, J. (2002a). Correlation models of diffuse solar-radiation applied to the city of São Paulo, Brazil. *Appl. Energy* 71, 59–73. doi:10.1016/s0306-2619(01)00040-x
- Oliveira, A., Machado, A., Escobedo, J., and Soares, J. (2002b). Diurnal evolution of solar radiation at the surface in the city of s/ao paulo: seasonal variation and modeling. *Theor. Appl. Climatol.* 71, 213–250. doi:10.1007/s007040200007
- Page, J. (1977). *The Estimation of monthly mean Value of daily short wave Irradiation on Vertical and inclined Surfaces from sunshine Records for latitudes 60°N to 40°S*. Department of Building Science, University of Sheffield, UK.
- Peel, M., Finlayson, B., and McMahon, T. (2007). Updated world map of the Köppen-Geiger climate classification. *Hydrol. Earth Syst. Sci.* 11, 1633–1644. doi:10.5194/hess-11-1633-2007
- Pereira, E., Martins, F., Abreu, S., and Colle, S. (2006). Brazilian atlas for solar energy resource: swera results, são josé dos campos. *INPE* 01, 60.
- Perez, R., Ineichen, P., Maxwell, E., Seals, R., and Zelenka, A. (1992). Dynamic global to direct irradiance conversion models. *ASHRAE Trans.* 98, 354–369.
- Perez, R., Ineichen, P., Seals, R., and Zelenka, A. (1990). Making full use of the clearness index for parameterizing hourly insolation conditions. *Sol. energy* 45, 111–114. doi:10.1016/0038-092x(90)90036-c
- Piazena, H. (1996). The effect of altitude upon the solar uv-b and uv-a irradiance in the tropical chilean andes. *Sol. Energy* 57, 133–140. doi:10.1016/s0038-092x(96)00049-7
- Podestá, G., Núñez, L., Villanueva, C., and Skansi, M. (2004). Estimating daily solar radiation in the argentine pampas. *Agric. For. meteorology* 123, 41–53. doi:10.1016/j.agrformet.2003.11.002

- Redweik, P., Catita, C., and Brito, M. (2013). Solar energy potential on roofs and facades in an urban landscape. *Sol. Energy* 97, 332–341. doi:10.1016/j.solener.2013.08.036
- Reindl, D., Beckman, W., and Duffie, J. (1990). Diffuse fraction correlations. *Sol. Energy* 45, 1–7. doi:10.1016/0038-092x(90)90060-p
- REN21 (2023). *Renewables 2023—global status report*. Available online: <https://www.ren21.net/global-status-report-2023/>
- Ridley, B., Boland, J., and Lauret, P. (2010). Modelling of diffuse solar fraction with multiple predictors. *Renew. Energy* 35, 478–483. doi:10.1016/j.renene.2009.07.018
- Rodríguez-Hidalgo, M., Rodríguez-Aumente, P., Lecuona, A., Legrand, M., and Ventas, R. (2012). Domestic hot water consumption vs. solar thermal energy storage: the optimum size of the storage tank. *Appl. Energy* 97, 897–906. doi:10.1016/j.apenergy.2011.12.088
- Saluja, G., Muneer, T., and Smith, M. (1988). Methods for estimating solar irradiation on a horizontal surface. *Ambient. Energy* 9, 59–74. doi:10.1080/01430750.1988.9675915
- Saluja, G., and Robertson, P. (1983). *Design of passive solar heating in the northern latitude locations*. Perth: Proc. Solar World Congress, 40.
- Sayigh, A. (2020). *Solar and wind energy will supply more than 50electricity by 2030* Berlin/Heidelberg, Germany: Springer, 385–399.
- Silva, Y., Takahashi, K., and Chavez, R. (2008). Dry and wet rainy seasons in the mantaro river basin (central peruvian andes). *Adv. Geosci.* 14, 261–264. doi:10.5194/adgeo-14-261-2008
- Silva, Y., and Trasmonte, G. (2010). *Variabilidad de las lluvias en el valle del Mantaro Memoria del Subproyecto: Pronóstico estacional de lluvias y temperatura en la cuenca del río Mantaro para su aplicación en la agricultura (Fondo Editorial CONAM-Instituto Geofísico del Perú)*. primera edn.
- Skartveit, A., and Olseth, J. (1987). A model for the diffuse fraction of hourly global radiation. *Sol. Energy* 38, 271–274. doi:10.1016/0038-092x(87)90049-1
- Skartveit, A., Olseth, J., and Tuf, M. (1998). An hourly diffuse fraction model with correction for variability and surface albedo. *Sol. Energy* 63, 173–183. doi:10.1016/s0038-092x(98)00067-x
- Smietana, P., Flocchini, R., Kennedy, R., and Hatfield, H. (1984). A new look at the correlation of Kd and Kt ratios and at global solar radiation tilt models using one-minute measurements. *Sol. Energy* 32, 99–107. doi:10.1016/0038-092x(84)90053-7
- Suárez Salas, L., Flores-Rojas, J. L., Pereira Filho, A. J., and Karam, H. (2017). Ultraviolet solar radiation in the tropical central Andes (12.0°S). *Photochem. Photobiol. Sci.* 16, 954–971. doi:10.1039/c6pp00161k
- Supit, I., and Van Kappel, R. (1998). A simple method to estimate global radiation. *Sol. Energy* 63, 147–160. doi:10.1016/s0038-092x(98)00068-1
- Turton, S. (1987). The relationship between total irradiation and sunshine duration in the humid tropics. *Sol. Energy* 38, 353–354. doi:10.1016/0038-092x(87)90007-7
- Vuilleumier, L., Hauser, M., Felix, C., Vignola, F., Blanc, P., Kazantzidis, A., et al. (2014). Accuracy of ground surface broadband shortwave radiation monitoring. *J. Geophys. Res. Atmos.* 119, 13838–13860. doi:10.1002/2014jd022335
- Whillier, A. (1956). The determination of hourly values of total solar radiation from daily summations. *Arch. Metall. Geoph. Biokl.* 7, 197–204. doi:10.1007/bf02243322
- Woodward, F., and Sheeh, J. (1983). *Principles and measurements in environmental biology*. London: Butterworth Co, 263.
- Younes, S., Claywell, R., and Muneer, T. (2005). Quality control of solar radiation data: present status and proposed new approaches. *Energy* 30, 1533–1549. doi:10.1016/j.energy.2004.04.031
- Zaratti, F., Forno, R. N., García Fuentes, J., and Andrade, M. (2003). Erythemally weighted uv variations at two high-altitude locations. *J. Geophys. Res. Atmos.* 108. doi:10.1029/2001jd000918

Glossary

Irradiance variables

E_T	extraterrestrial solar irradiance ($W\ m^{-2}$)
E_T^h	hourly value of extraterrestrial solar irradiance at the surface ($MJ\ m^{-2}\ hour^{-1}$)
E_T^d	daily value of extraterrestrial solar irradiance at the surface ($MJ\ m^{-2}\ day^{-1}$)
E_G	global solar irradiance ($W\ m^{-2}$)
E_G^h	hourly value of global solar irradiance at the surface ($MJ\ m^{-2}\ hour^{-1}$)
E_G^d	daily value of global solar irradiance at the surface ($MJ\ m^{-2}\ day^{-1}$)
E_{DR}	direct solar irradiance ($W\ m^{-2}$)
E_{DR}^h	hourly value of direct solar irradiance at the surface ($MJ\ m^{-2}\ hour^{-1}$)
E_{DR}^d	daily value of direct solar irradiance at the surface ($MJ\ m^{-2}\ day^{-1}$)
E_{DF}	diffuse solar irradiance ($W\ m^{-2}$)
E_{DF}^h	hourly value of diffuse solar irradiance at the surface ($MJ\ m^{-2}\ hour^{-1}$)
E_{DF}^d	daily value of diffuse solar irradiance at the surface ($MJ\ m^{-2}\ day^{-1}$)
K_T	clearness index (nondimensional)
K_T^h	hourly value of clearness index (nondimensional)
K_T^d	daily value of clearness index (nondimensional)
K_D	diffuse fraction of the solar irradiance (nondimensional)
K_D^h	hourly value of diffuse fraction of the solar irradiance (nondimensional)
K_D^d	daily value of diffuse fraction of the solar irradiance (nondimensional)

Atmospheric variables

q	specific humidity ($g\ kg^{-1}$)
T	air temperature ($^{\circ}C$)
RH	relative humidity (%)
S	monthly average daily value of sunshine hours (hours)
S_{max}	maximum monthly average daily value of sunshine hours (hours)

Statistical Parameters

MBE	mean bias error
R^2	coefficient of determination
$RMSE$	root mean square error
AIC	Akaike's information criterion
$\Delta_i AIC$	difference of Akaike's information criterion

Empirical Irradiation models

$MADHG$	Monthly-averaged daily horizontal global
$MADHD$	Monthly-averaged daily horizontal diffuse

$DAHG$	Daily-averaged horizontal global
$DAHD$	Daily-averaged horizontal diffuse
HHG	Hourly horizontal global
HHD	Hourly horizontal diffuse
HDC	Hourly diffuse correlation